Measurement of Σ^+p Elastic Scattering with Scintillating Fiber Target

Yuji Goto

Abstract

The differential cross section of Σ^+p elastic scattering has been measured in the Σ^+ momentum region of 300 – 600 MeV/c. The measurement has been performed with use of a novel visual-image detector system consisting of a scintillating-fiber (SCIFI) target and a pair of image-intensifier tubes. The separated π^+ beams of 1.64 GeV/c and the scattered K^+'s have been detected with the spectrometers to trigger the hyperon productions on-line and to select the missing mass peak of Σ^+ productions off-line. The SCIFI-target system has provided digitized pictures showing Σ^+ productions via the reaction $\pi^+ + p \rightarrow K^+ + \Sigma^+$ followed by decay and/or scattering of the Σ^+'s. For the analysis of the image data, a track recognition program has been developed to pick up automatically the event topologies of Σ^+ decay and scattering. The track recognition program has reduced effectively the number of background events to be scanned by human eyes. We have established a new method to measure hyperon-nucleon scatterings in the energy region where the cross section were hardly measured before. The obtained cross sections, $2.2^{+3.2}_{-1.1}$ (mb/sr)($-0.4 \leq \cos\theta_{CM} < 0.1$) and $3.3^{+2.5}_{-1.2}$ (mb/sr)($0.1 \leq \cos\theta_{CM} < 0.6$), are consistent with the prediction of the Nijmegen hard-core models and the quark-cluster model by a Kyoto-Niigata group. The technical details are described and the future direction is indicated.

1. Introduction

Studies of baryon-baryon (BB) scatterings including hyperons are essential for complete understanding of the strong force. In the non–strange sector, nucleon–nucleon (NN) scatterings have been studied extensively. The wide energy region has been covered with abundant data on differential and total cross sections and spin observables of NN scatterings. Beyond phenomenological understanding on the property of the nuclear force, one-boson-exchange (OBE) models [1, 2, 3] have well described these data and have successfully given a microscopic view of the nuclear force. If sufficient data on hyperon–nucleon (YN) scattering as well as on NN scattering are available, we can give the complete description of BB interaction and show fundamental aspects of the strong interaction. In particular, we can answer remaining problems, e.g. short-range repulsive force and spin–orbit force. However, there exist very little data on the cross section for YN scattering only in low energy region. They were obtained by bubble chamber experiments in the 1960's [4, 5, 6, 7, 8, 9, 10]. No additional data have been taken for more than twenty years since then.

The NN scattering data are well described with OBE models. The models can be extended to YN scattering. A Nijmegen group extended their model on the NN interaction to the YN interaction with use of the flavor SU(3) symmetry [11, 12, 13]. A Bonn–Jülich

group developed a model based on the SU(6) symmetry [14, 15]. In their models, the SU(3) and the SU(6) symmetries were used for obtaining coupling constants for meson–baryon coupling vertices.

The most characteristic difference among these models is in their treatment of short-range repulsive force. The Nijmegen group proposed two types of the repulsive force. One of them is a phenomenological hard-core. They proposed also a soft-core model in which a Gaussian-type potential was used accounting to the exchange of the Regge trajectories. In the Bonn–Jülich model, the repulsive force is due to ω-meson exchange. These models were tuned to reproduce the existing NN and YN scattering data. Due to the scarce experimental data in YN channels, however, various theoretical assumptions on the model parameters were required. As the results the models predicted different aspects in the energy region where no experiment on YN scattering had been done. For example, the Nijmegen hard-core model predicted strong enhancement of p-wave contribution to the Σ^+p channel in the momentum region of several hundred MeV/c, whereas it is not the case for other models. In any case, in the OBE models, the magnitude of short-range repulsion is obtained by introducing phenomenological cutoffs. It is desirable that the short-range repulsive force is described with more fundamental manner.

At a short distance, baryons overlap each other and the property should be described with underlying degrees of freedom, that is quarks and gluons. This problem is related to the understanding of the non-perturbative regime of QCD. The groups from Tokyo [16, 17, 18], Tübingen [19, 20] and Kyoto–Niigata [21, 22, 23, 24] independently made an approach to this problem with use of quark-cluster models (QCM) based on the resonating group method (RGM) with antisymmetrized six-quark wave functions.

In their models, the potential V_{ij} between the i-th quark and the j-th quark consists of the confinement term V_{ij}^{conf} and the residual one-gluon-exchange (OGE) potential V_{ij}^{OGE};

$$V_{ij} = V_{ij}^{conf} + V_{ij}^{OGE}.$$

The confinement term is supposed to represent non-perturbative effects of QCD and describes the confinement of quarks in a color-singlet hadron. The short-range repulsion naturally arises from Pauli principle by the antisymmetrization of quarks and the color-magnetic interaction term in the OGE potential.

Dover and Feshbach examined in the references [25, 26] how the flavor SU(3) symmetry is broken in the OBE model and QCM. In the OBE model, the flavor SU(3) symmetry is applied to the meson–baryon coupling constants, while physical masses of baryons and mesons are used. Due to the mass differences among baryons and those among mesons, the flavor SU(3) symmetry is broken dynamically. They showed that some of the SU(3) relations are still well satisfied in spite of the SU(3) breaking. Such kind of approach manifests the mechanisms of SU(3) breaking in the BB interaction and leads to the understanding of non-perturbative regime of QCD.

Although progress in theoretical understanding of YN interaction has been made, new experimental data are desirable in order to select various models which are helpful for detailed understanding of strong interaction. For obtaining new experimental data, new technologies must be introduced.

The major difficulty to measure the cross sections for YN scatterings comes from short life-time of hyperons. For instance, $c\tau$ of Σ^+ is only 2.396 cm. To detect YN scattering in such a short life-time, the detector must be a production target for hyperons and at the same time a scattering target which provides a three-dimensional visual capability to recognize the complicated reaction sequence.

Bubble chambers were used as visual detectors for detecting YN scattering in 1960's. Table 1 shows a compilation of YN scattering data which were obtained with bubble chambers in 1960's. Relatively good statistics were acquired in the experiments using the 81-cm hydrogen-bubble-chamber with stopped K^-'s at CERN-PS [4, 5, 6, 9]. However, observed energy regions were limited since the momenta of hyperons produced with stopped K^-'s were low.

YN channel	number of events	momentum (MeV/c)	reference
Λp elastic	378	120 - 320	[5]
Λp elastic	224	120 - 330	[6]
Λp elastic	131	500 - 4000	[7]
Λp inelastic	52	600 - 4000	[7]
Λp elastic	175	200 - 2000	[8]
Λp inelastic	61	600 - 2000	[8]
Λp elastic	584	400 - 10000	[10]
Λp inelastic	408	1200 - 10000	[10]
$\Sigma^- p$ inelastic	411	105 - 165	[4]
$\Sigma^- p$ elastic	21	500 - 4000	[7]
$\Sigma^- p$ inelastic	406	130 - 170	[9]
$\Sigma^+ p$ elastic	22	500 - 4000	[7]
$\Sigma^+ p$ elastic	121	140 - 180	[9]

Table 1: A compilation of YN scattering data which were obtained with bubble chambers in 1960's.

To make an experimental breakthrough in this field of physics, we have started an experimental project to perform series of YN scattering experiments by a new technology using the scintillating-fiber detector. In this paper we describe the first attempt to measure the cross section for $\Sigma^+ p$ elastic scattering in the energy region where no experimental data have been taken. We owe the present experiment to the technical advances described below.

1. We have used thin scintillating fibers (SCIFI) with the cross section of $500\mu m \times 500\mu m$ square. The number of photons from the fiber has been about 6 per fiber for a minimum ionizing particle. We have developed a SCIFI block with the volume of $8 \times 8 \times 10 cm^3$. The fiber sheets which have consisted of layers of 160 fibers have been stacked in two orthogonal directions alternately. The photons from this block can be readout in the two orthogonal directions. A pair of image-intensifier tubes (I.I.T.) with the aperture of 8cm ϕ combined with a CCD camera have

been used for reading the signals from the SCIFI block. The signal from the CCD cameras has been digitized in real-time, and recorded as digital image data. With use of the image data in the two directions, particle trajectories in the SCIFI block have been able to be reconstructed three-dimensionally. Combining these techniques, we have realized a novel visual detector.

2. The above I.I.T. system is triggered by external signals from the beam line and spectrometer which select the events of hyperon production.
3. For the analysis of image data from the visual SCIFI detector, an automatic-tracking program has been developed. By recognizing the event pattern in the SCIFI detector automatically, the number of events to be scanned by human eyes can be reduced substantially.

The experiment has been performed at KEK-PS. The Σ^+'s have been produced with 1.64-GeV/c π^+ beam in the process;

$$\pi^+ + (p) \rightarrow K^+ + \Sigma^+ ,$$

where (p) means a proton in polystyrene ($(CH)_n$) of scintillating fiber. The high resolution spectrometer which is located downstream of the SCIFI target and covers the forward region identifies the produced K^+. The Σ^+'s produced on hydrogens have momenta which can be calculated by means of the analysis of beam momenta and the production angles. The momentum region covered in this experiment is from 400 MeV/c to 500 MeV/c. Although the momentum of Σ^+ produced in a carbon nucleus cannot be determined kinematically because of the Fermi motion of protons in the nucleus and has uncertainty spread out from 300 MeV/c to 600 MeV/c, we can utilize these Σ^+'s by a complete recognition of the topology of all the tracks of the event. The Σ^+ is identified by recognizing its decay in the SCIFI detector which appears as a kink. The $\Sigma^+ p$ elastic scattering on a free proton;

$$\Sigma^+ + p \rightarrow \Sigma^+ + p ,$$

is identified by observing the recoil proton which appears as a branch and followed by Σ^+ decay. The SCIFI detector serves both as the production target and as the scattering target.

One of the features of the present experiment is to acquire the data in the momentum region which had not been able to be observed with bubble chamber due to the statistics. For this purpose the off-line event reduction using an automatic track-recognition is indispensable. The automatic-tracking program which identifies Σ^+ production and its decay reduces the number of background events before scanning by human eyes. Our visual detector provides digitized data which can be directly processed with a computer. To find tracks in the image data, we have introduced the method of "Hough transformation" [27, 28]. We have reduced the number of events to be scanned by human eyes by means of the automatic-tracking program. The cross section for $\Sigma^+ p$ elastic scattering has been derived for the momentum region of Σ^+ from 300 MeV/c to 600 MeV/c. In this momentum region, the Nijmegen models and the Kyoto–Niigata quark-cluster model have predicted different

angular distributions and the absolute values of the cross section. Our results have been compared with these theoretical calculations.

In Chapter 2, the experimental method and the instruments used in the experiment are described. Chapter 3 presents the procedures of the data analysis. The performance of the SCIFI detector is evaluated and the procedures of the image data analysis is validated. In Chapter 4, the cross section for the $\Sigma^+ p$ scattering is derived and in Chapter 5 the results are presented and discussed. The conclusion is given in Chapter 6.

2. Experimental Procedure

The present experiment was performed with the K2 beam line of 12-GeV Proton Synchrotron (PS) at KEK. The π^+ beam was used to produce Σ^+'s in the (π^+,K^+) reaction, and scatterings of the Σ^+ were observed in the scintillating fiber (SCIFI) target. Figure 1 shows a top view of the experimental setup consisting of the beam line, the K^+ spectrometer and the SCIFI-target system. They were also used in the previous H-dibaryon search experiment [29, 30, 31]. The (π^+,K^+) reaction was identified with the beam line and the K^+ spectrometer. The Σ^+ produced in the reaction was observed as a track in the SCIFI target. The momentum region of the Σ^+ was 300 MeV/c to 600 MeV/c. The Σ^+p elastic scatterings were found also in the SCIFI target by identifying the Σ^+ track and the recoil proton track. Details of the experimental setup are described in references [32] and [33]

2.1 Beam Line

The proton beam was extracted from KEK-PS in the slow extraction mode during two

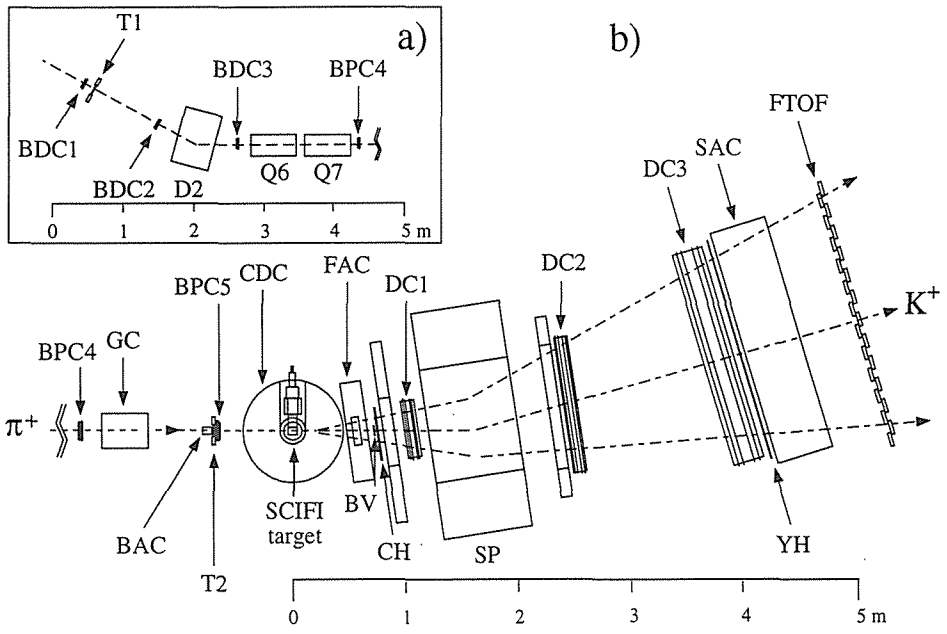

Figure 1: Top view of the experimental setup.

seconds (spill) with a two-second interval. The beam was transported to hit a platinum primary target. The secondary particles produced in the direction of 0 degree were transported through the K2 beam line [34]. The schematic view of the K2 beam line is shown in Fig. 2.

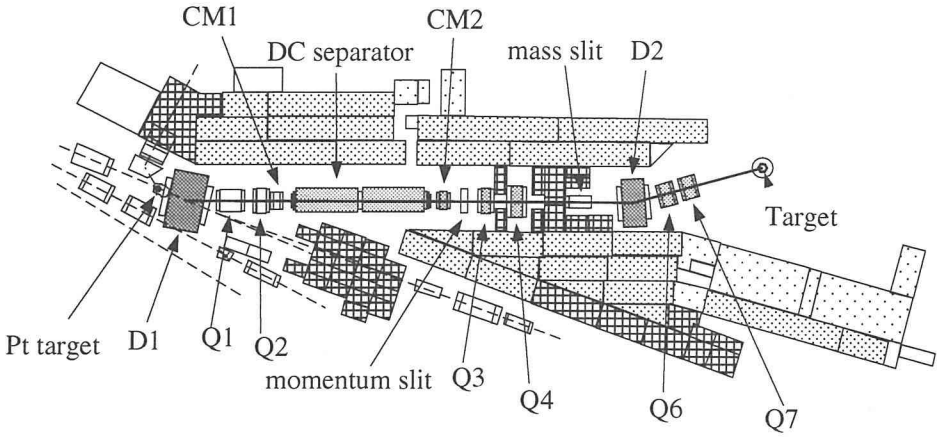

Figure 2: Top view of the K2 beam line.

The secondary particles were bent with the dipole magnet D1 by 23 degrees. The quadrupole magnets Q1 and Q2 made the beam direction horizontal, that is perpendicular to the electric field in the DC separator and focused the beam horizontally at the momentum slit. The beam passed through the DC separator of 6-m long which had electrodes with 10-cm gap providing electrostatic field of 55 kV/cm vertically. The trajectories of particles were split in respect of the mass with the DC separator, and then vertically focused with the quadrupole magnets Q3 and Q4 at the position of the mass slit. The vertical position of the π^+ at the mass slit was adjusted by the correction magnets (CM1 and CM2). Finally, the beam was bent with the dipole magnet D2 by 15 degrees and focused on the SCIFI target by the quadrupole magnets Q6 and Q7. The total length of the beam line from the primary target to the final focal point was about 25.8 m.

The central value of the beam momentum was tuned to 1.64 GeV/c. The typical beam intensity was 1×10^5 /spill. On the typical condition, the contaminations of e^+ and μ^+ in the beam was about 7 % in total, and those of K^+ and proton were less than 1 %.

The particle identification and the momentum determination of the beam particles were performed with two scintillation counters (T1 and T2), a silica aerogel Čerenkov counter (BAC), a gas Čerenkov counter (GC), three sets of drift chambers (BDC1, BDC2 and BDC3) and two sets of multi-wire proportional chambers (BPC4 and BPC5).

The T1 and T2 were used for the time-of-flight analysis for the particle identification. The T2 also served as the start counter which determined the trigger timing. The T1 and T2 were made of plastic scintillators (NE pilot-U), the sizes of which were 5-mm thick, 5-cm high, and 10-cm and 5-cm wide. Each of them was viewed horizontally by fast phototubes (Hamamatsu R2083) from both sides. The counters were located 6-m apart from each other. The obtained time-of-flight resolution was 85 psec (r.m.s.).

The BAC was used to tag π^+'s and lighter particles in the beam and to exclude heavier

particles. The size of the silica aerogel was 3-cm thick, 8-cm high and 8-cm wide. It had a refractive index of 1.03 which corresponded to the β threshold of 0.971 for the Čerenkov radiation and discriminated 1.64-GeV/c π^+ ($\beta = 0.996$) from K^+ ($\beta = 0.958$) or heavier particles. The Čerenkov light was detected with a 5-inch photo-tube (Hamamatsu R1250). The detection efficiency for the 1.64-GeV/c π^+ was 99.6 %.

The GC vetoed lighter particles than π^+ in the beam. It contained freon-12 (CCl_2F_2) as radiator gas. The pressure was set to 3.5 atm in order to eliminate e^+'s and μ^+'s.

The BDC1 and BDC2 were located upstream of the D2 magnet, and the BDC3 was located downstream of it. Each of them had two planes, X and X′, whose cell structure is shown in Fig. 3. The effective area of the BDC1 was 16-cm wide and 11-cm high. The effective areas of the BDC2 and BDC3 were 16-cm wide and 15.5-cm high. Their specifications are summarized in Table 2. Mixed gas of argon (80%) and isobutane (20%) was used. The efficiencies were better than 99.9 % for the 1.64-GeV/c π^+, and the obtained position resolutions were 230 μm for the BDC1, 150 μm for the BDC2 and 170 μm for

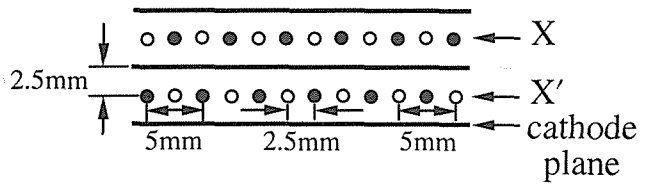

Figure 3: The cell structure of BDC's. Closed and open circles represent sense wires and potential wires respectively.

BDC	BDC1	BDC2	BDC3
planes	X X′	X X′	X X′
number of anode wires	32	32	32
spacing between anode wires (mm)	5	5	5
diameter of anode wire (μm)	10	12	10
H.V. on potential wire (V)	−1500	−1450	−1500
H.V. on cathode plane (V)	−1450	−1400	−1450
dimension X×Y (mm)	160×110	160×155	160×155

Table 2: The structure and operational condition of BDC's.

the BDC3.

The BPC4 and BPC5 which were located downstream of Q7 were used together with BDC's for the momentum measurement. Each of them had X and Y planes of 1-mm spacing anode wires. The "magic gas", that is the mixture of argon, isobutane, freon-13B1 (CF_3Br) and methylal were used. The H.V. of about 4 kV were applied to the BPC's.

The cylindrical drift chamber (CDC) described in Section 2.2.3 was also used for the beam tracking incident to the SCIFI target.

2.2 K^+ Spectrometer

2.2.1 Spectrometer Magnet

The spectrometer magnet (SP) was a window-frame type dipole-magnet. It had a pole gap of 50-cm high, 100-cm wide and 80-cm long. The 8-cm thick end-guard plates were located 80-cm from the center of the magnet.

The magnet center was located 150-cm downstream of the target center along the beam axis. The direction of the magnet was rotated by 0.15 radian with respect to the beam direction. The field strength was 1.1 T at the center of the magnet and $B \cdot dl$ was about 1.08 T·m for the particles with momentum between 0.8 GeV/c and 1.3 GeV/c.

2.2.2 Tracking Drift Chambers

The momenta of outgoing particles were measured with three sets of drift chambers placed upstream (DC1) and downstream (DC2 and DC3) of the SP magnet.

The DC1 was located just downstream of the front end-guard of the SP magnet. The effective area of DC1 was 50-cm width × 35-cm height. It had two X planes, one Y plane and one U plane. The cell structure of the DC1 is shown in Fig. 4 a). Anode wires of U

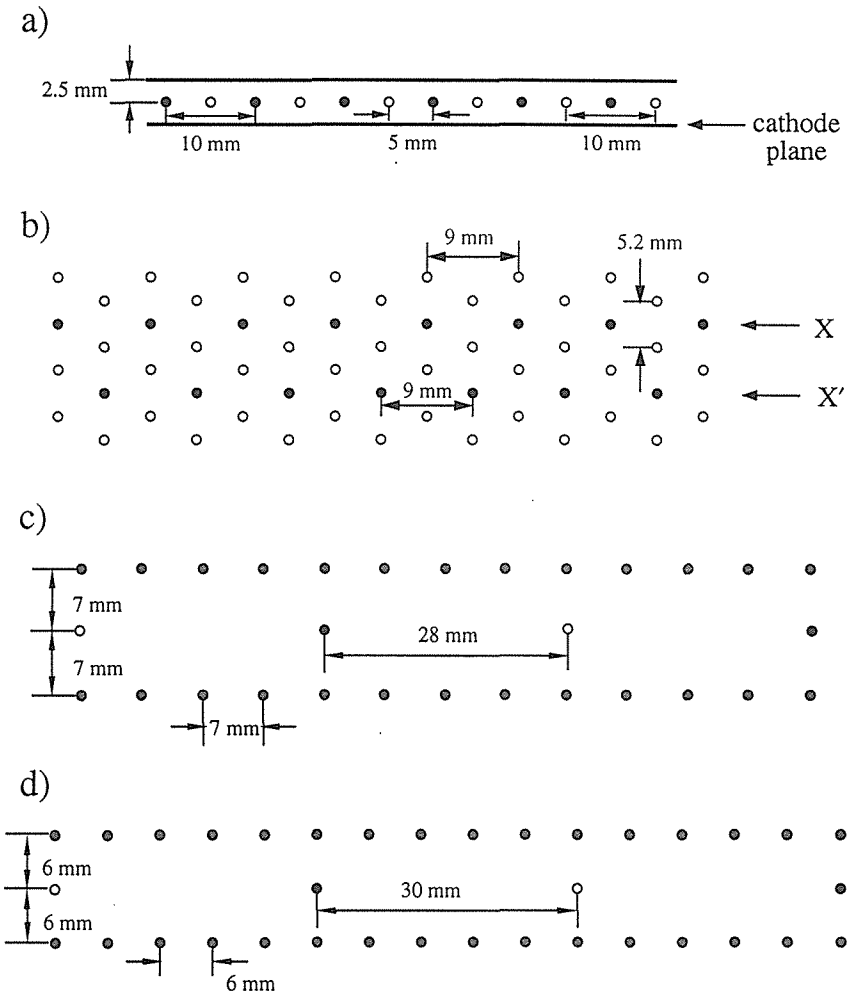

Figure 4: The cell structures of a) DC1, b) DC2, c) X, X′ planes of DC3 and d) Y, Y′ planes of DC3. Closed circles, open circles and hatched circles represent sense wires, potential wires and field shaping wires respectively.

plane were tilted by 15 degrees from the vertical direction. The typical efficiency was 99.5 % and the obtained position resolutions were 220 μm for the X planes, 400 μm for the Y plane and 200 μm for the U plane.

The DC2 and DC3 were located downstream of the magnet. Each of them had two X planes and two Y planes. Figures 4 b), c) and d) show the cell structures of DC2, and the X, X′ planes and Y, Y′ planes of DC3 respectively. The DC2 had the effective area of 120 cm × 120 cm. The typical efficiency was 90.3 % and the position resolutions were 230 μm for the X planes and 270 μm for the Y planes. The DC3 had a sensitive area of 180-cm wide and 90-cm high. The typical efficiency was 93.5 % and the position resolutions were 310 μm for the X planes and 390 μm for the Y planes.

Mixed gas of argon (50%) and ethane (50%) was used for DC1, DC2 and DC3. The structure and the operational condition are summarized in Table 3.

DC	DC1	DC2	DC3
planes	X X′ Y U	X X′ Y Y′	X X′ Y Y′
number of anode wires	XX′:48 Y:32 U:40	XX′:128 YY′:96	XX′:32 YY′:16
spacing between anode wires (mm)	10	9	XX′:56 YY′:60
diameter of anode wire (μm)	20	20	20
potential on anode wire (V)	-	-	+950
H.V. on potential wire (V)	−1950	−2100	−3000
H.V. on cathode plane (V)	−1800	-	-
dimension X×Y (mm)	500×350	1200×1200	1800×900

Table 3: The structure and operational condition of DC's.

2.2.3 Cylindrical Drift Chamber

The cylindrical drift chamber (CDC) surrounding the SCIFI target had eight cylindrical layers of drift cells as described in Table 4. The radius of the inner-most layer was 16 cm and that of the outer-most layer was 38.4 cm. The height of the effective area was 90 cm. It had two stereo layers tilted by 5.71 degrees from the vertical direction. The typical efficiencies were from 93 % to 96 % and the position resolutions were about 270 μm. All the cells had the identical structure with drift space of 11.2 mm as shown in Fig. 5. The voltages supplied to the cathode wires were −2260 V and −2510 V as shown in the figure. Mixed gas of argon (50%) and ethane (50%) was used for operation. The incident beam particles were traced to the target from the positions on the CDC and the BPC's. The outgoing particles from the target were traced from the CDC, DC1, DC2 and DC3.

Layer	1	2	3	4	5	6	7	8
position of anode wires from the center (mm)	160.0	192.0	224.0	256.0	288.0	320.0	352.0	384.0
number of anode wires readout	32	42	48	60	69	76	87	97
direction of wire	Y	Y	stereo	Y	Y	stereo	Y	Y

Table 4: The structure of CDC.

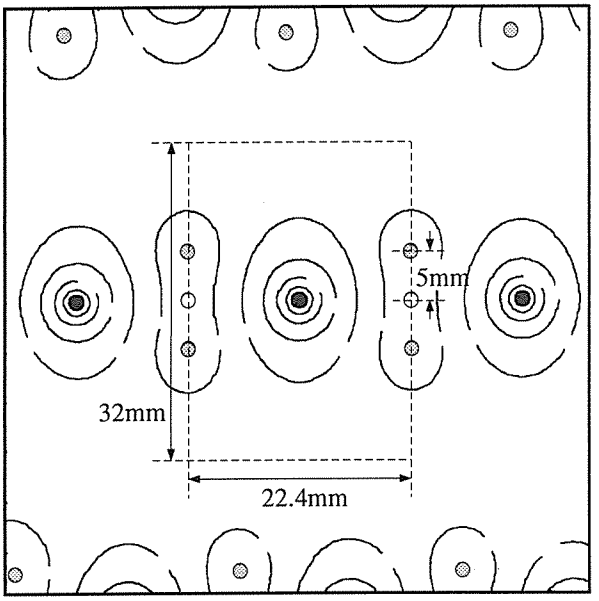

Figure 5: The cell structure of the CDC with the simulated shapes of the field. Closed circles represent anode wires. Open and hatched circles represent cathode wires to which voltages of -2260 V and -2510 V were supplied respectively.

2.24 Forward TOF Hodoscope

For particle identification of K^+, the velocities of particles were determined by the time-of-flight between the start counter T2 and the forward TOF hodoscope (FTOF). The flight length was measured with the drift chambers. The FTOF consisted of twenty-four scintillators which were 12-cm wide and 3-cm thick. The height was 130 cm for the central ten counters and 110 cm for the others. Each of them was viewed by photo-tubes (Hamamatsu H1949) from the top and the bottom end. The time-of-flight resolution was 110 psec (r.m.s.). The FTOF provided also the vertical hit position by the time difference between the signals from the both ends. The position resolution was 14.8 mm (r.m.s.).

2.2.5 Silica Aerogel Čerenkov Counters

For K^+ tagging, major backgrounds were π^+ and proton. In order to reduce the contamination of π^+, two sets of aerogel Čerenkov counters (FAC and SAC) were installed. The FAC was located between the SCIFI target and the SP magnet. The SAC was located downstream of the DC3.

The FAC was made of silica aerogel with refractive index of 1.03. Two pieces of aerogel which had the size of 3-cm thick, 25-cm high and 35-cm wide were installed in the diffusion box whose inner surface was covered with white reflector (Millipore). They were located on the beam axis. The Čerenkov light was viewed from both the left and the right sides with two photo-tubes (Hamamatsu R1250). The FAC eliminated 95 % of π^+ in the momentum range of interest.

The SAC consisted of silica aerogel whose refractive index was 1.041. Three pieces of aerogel whose sizes were $20 \times 20 \times 3$ cm^3 were stacked to form a 9-cm-thick block. The

effective area of 100-cm high and 200-cm wide was covered with these blocks. The inner surface of the SAC box was covered with Millipore. The Čerenkov light was detected with thirty-eight photo-tubes (Hamamatsu R1250 and RCA 8854) from the top and the bottom. The β threshold for the Čerenkov radiation was 0.961 which distinguished K^+'s from π^+'s in the momentum range between 0.5 GeV/c and 1.5 GeV/c.

By using both the FAC and SAC, 99.5 % of π^+'s were eliminated in the trigger signals. The detection efficiency for K^+ was 95 %.

2.2.6 Other Trigger Counters

To eliminate the contamination of the π^+ beam in the trigger, the beam veto counter (BV) was located on the beam axis between the FAC and the SP magnet. The size of BV was 0.6-cm thick, 8-cm high and 8-cm wide, providing the veto region of ± 0.06 radian in the horizontal and the vertical directions.

A hodoscope (CH) was installed upstream of the SP magnet, just outside of the end-guard. The CH consisted of horizontally arranged twelve scintillators each of which was 1-mm thick, 17-cm high and 3.5-cm wide. It was used for the first-level trigger combined with the FTOF to eliminate negative particles and to select roughly the momentum region of the positively charged particles by means of the matrix coincidence method (see Section 2.5.1). It was also used for the second-level trigger to provide the momentum information for the "mass-trigger" (see Section 2.5.2).

Another hodoscope (YH) was installed just upstream of the SAC. The YH consisted of vertically arranged six scintillators each of which was 0.4-cm thick, 16-cm high and 196-cm wide. This hodoscope was used to eliminate fake-triggers due to neutral particles. It defined the acceptance of the spectrometer system.

2.3 Scintillating-Fiber-Target System

2.3.1 SCIFI Target

The scintillating fiber (SCIFI) target was a visual detector located at the focal point of the beam. It consisted of plastic scintillating fibers, SF81 (KURARAY). The scintillating fibers were 20-cm long and had a 500 μm $\times$ 500 μm-square cross section. The core of the fiber was 480 μm $\times$ 480 μm square which was coated with a clad of 10-μm thick. The core material was polystyrene ($(CH)_n$) which had refractive index of 1.59 and density of 1.06 g/cm^3. The clad was made of polymethylmethacralate (PMMA, $C_5H_8O_2$) which had a refractive index of 1.49 and density of 1.18 g/cm^3. The wave length of induced photon has a peak at 437 nm.

Figure 6 shows a schematic view of the SCIFI target. The fibers were bundled to make a 8-cm-wide fiber sheet by placing the 160 fibers in a row. The SCIFI sheets were stacked alternately in the vertical direction and in the horizontal direction, providing the target volume of 8 cm $\times$ 8 cm $\times$ 10 cm. The number of stacked sheets was 92 for each direction. The sheets were glued with black epoxy which also worked as extra mural absorber (EMA) to eliminate cross talks of photons over the sheets. The average thickness of the glue was 50 μm. The spaces between the fiber sheets for each direction were reduced from 550 μm to 350 μm in the readout arms in order to make the fiducial size viewed by the I.I.T.'s (8 cm ϕ) larger. A plate with holes were attached at the other end of fiber block. LED light through the holes provided the position reference as described in Section 2.4.1.

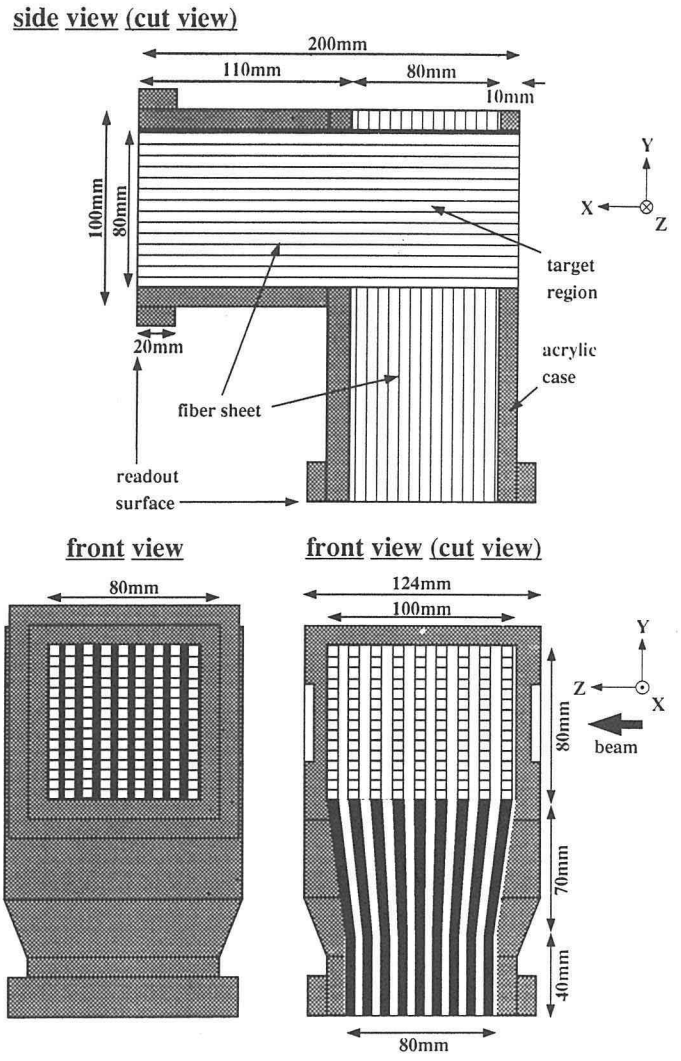

Figure 6: Schematic view of the SCIFI target.

2.3.2 Image-Intensifier Tube

The photon output from the SCIFI target was amplified with two sets of I.I.T.'s (DELFT PP0040C), one for the X-Z plane viewed from the vertical direction, and the other for the Y-Z plane viewed from the horizontal direction. The I.I.T. was an assembly of three stages of independent image intensifiers. A schematic view of the I.I.T. system is shown in Fig. 7. The first stage was an electrostatic type of image intensifier. The diameter of the input-window was 8 cm ϕ. The image was demagnified and focused on the output-window of 1.8 cm ϕ. Both the input-window and the output-window were made of glass fiber. The SCIFI target was put on the input-window with optical-grease. The photons from the SCIFI target were converted to electrons on the photo-cathode S20. The photo-

electron was accelerated and converted to photon again by bombarding the phosphor P24. The phosphor served as an optical delay keeping the image during its optical decay-time of 2.4 μsec. The second and third stages were the same type using a micro-channel-plate (MCP) with a diameter of 1.8 cm. Both the input-window and the output-window were made of glass-fiber. The photons were converted to electrons at the photo-cathode. The electrons were amplified with the MCP and converted to photons again with the phosphor P20. The operational conditions for all the stages are summarized in Table 5.

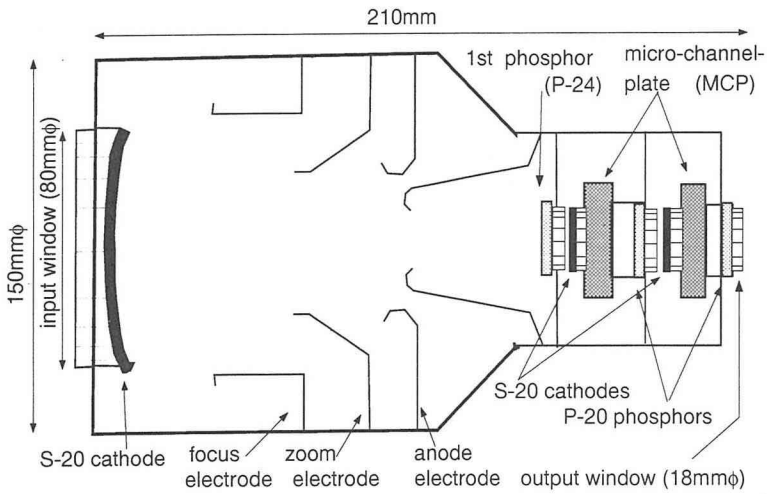

Figure 7: Schematic view of the I.I.T.

stage of I.I.T.	1st stage	2nd stage	3rd stage
voltage on image intensifier	20 kV	X:688V Y:698V	X:683V Y:695V
voltage on gate		$^{+50}_{-200}$V	$^{+50}_{-200}$V
width of gate	(D.C. operation)	2.5 μsec	1 msec
trigger		first-level	second-level
material of photo-cathode	S20	S20	S20
material of phosphor	P24	P20	P20
decay-time (1/10) of phosphor	2.4 μsec	50 μsec	50 μsec

Table 5: The decay-time of phosphor and the gate operation of image intensifiers.

The first stage was operated in DC mode with the cathode voltage of 20 kV. The photon amplification factor was about 8. Since all the photons from the SCIFI target were amplified on the first stage without selection, phosphor P24, which has short decay-time (2.4 μsec), was used to prevent overlapping with events produced by the beam particles which came earlier than the particles of interest.

The second stage and the third stage were gated by the first-level trigger (see Section 2.5.1) and the second-level trigger (see Section 2.5.2) respectively. The first-level trigger was made within 400 nsec after the interaction. The delay was shorter than the decay-time of phosphor P24 (2.4 μsec). In order to prevent overlapping with the events produced by the beam particles which came later, the gate width was set rather short (2.5 μsec). The

amplified image was held in phosphor P20 of the second stage which had the decay-time of 50 μsec. The second-level trigger was invoked within 15 μsec, and the output image of the second stage was amplified on the third stage. The gate width was 1 msec. Supplied voltages for the second and the third stages were determined to produce the equivalent light outputs from the two sets of I.I.T. system. The amplification factor for each stage was about 10^3.

2.3.3. CCD Video Camera

The photon image from the I.I.T. was viewed by a CCD camera through the optical lens system. The lens system consisted of lenses with the focal lengths of 135-mm and 50-mm coupled in tandem, where the 135-mm lens was attached reversely. It demagnified the image to 41 %. The CCD camera (SONY XC-77) had a CCD-chip containing 768 $\times$ 493 pixels. The size of the chip was 8.8 mm $\times$ 6.6 mm and that of each pixel was 11 μm $\times$ 13 μm. The output from the CCD camera was a video signal of the NTSC format.

2.34. Image Digitizer

The output video signal from the CCD camera was digitized in real-time with the image digitizer consisting of four NIM modules, a clock and coordinate generator module (CCG), a flash ADC module (FADC) and two sets of first-in-first-out buffer-memory modules (FIFO).

The CCG module provided a common clock to synchronize the readout of the two CCD cameras and the digitization with the FADC module, and generated two-dimensional coordinates for the corresponding CCD pixel. When the second-level trigger signal was accepted, the CCG module started the readout and the digitization. Since the start from the CCG module occurred every 1/60 second, the readout and the digitization process had effectively 25-msec dead-time. The FADC module had two sets of flash ADC's which digitized the pulse height of the video signal which was proportional to the brightness. The brightness was compared with the preset threshold value of the pulse height. When the brightness was larger than the threshold, the data was sent to the FIFO modules.

The FIFO module stored the two-dimensional coordinates generated by the CCG module, the brightness digitized by the FADC module and the event-number. The stored pixel data had the length of 32 bits which consisted of 10 bits and 9 bits for the two-dimensional coordinates respectively, 7 bits for the brightness and 6 bits for the event-number. A FIFO module stored the pixel data of the X-Z plane and the other one stored that of the Y-Z plane. Each FIFO module could store the data of 4K pixels. Since the typical data size for one event was 2K pixels for each direction, the FIFO module was readout by a VME I/O module when it was not empty.

24. Basic Performance of the SCIFI-Target System

The basic performance of the SCIFI-target system was investigated with 1.6-GeV/c minimum-ionizing π^+ beams. We describe also the necessary corrections for the intrinsic distortion of the present SCIFI-target system.

24.1 Calibration of the SCIFI Image Data

A pinhole distortion was caused by the electrical lens system of the first-stage image intensifier and the optical lens system to connect the I.I.T. to the CCD camera. The pinhole distortion has linear dependence on the distance from

the optical center, as expressed in the formula;

$$\begin{pmatrix} y' \\ z' \end{pmatrix} = (1 + ar) \begin{pmatrix} y - y_c \\ z - z_c \end{pmatrix} + \begin{pmatrix} y_c \\ z_c \end{pmatrix}.$$

Here, (y,z) is the real position and (y',z') is the position in the distorted image. The distortion is assumed to depend only on r, the distance from the optical center (y_c,z_c), i.e.;

$$r = \sqrt{(y - y_c)^2 + (z - z_c)^2}\,.$$

A coefficient a and the optical center (y_c,z_c) are the parameters to be determined to correct the distortion.

To find the optimum parameters, we utilized the sheet structure of the SCIFI target. The position of each SCIFI sheet was identified by plotting the center of photon cluster as shown in Fig. 8 a). In this picture, the images of many events are plotted together. The definition of a cluster is given in Section 2.4.2. The parameters were determined to make the sheet image straight. The corrected image is shown in Fig. 8 b).

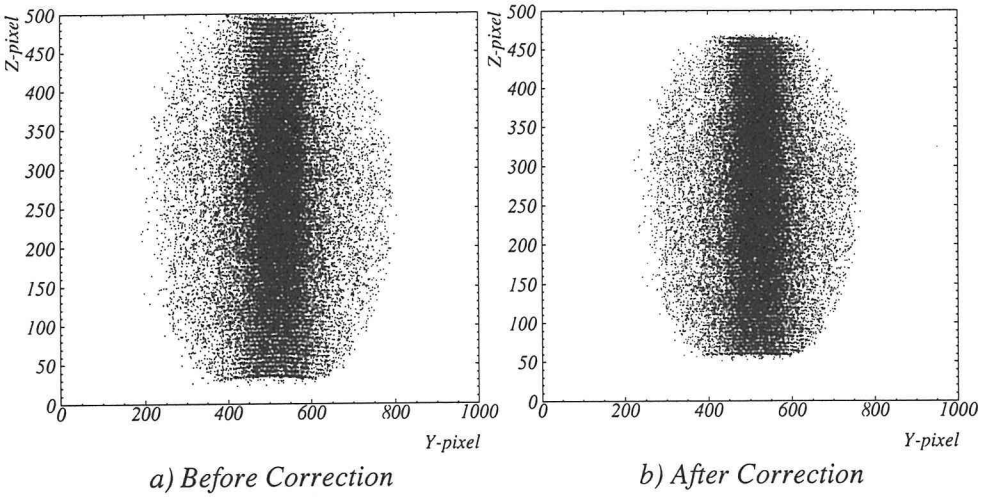

Figure 8: Distortion correction with the SCIFI sheets. Abscissas and ordinates show the pixel-number.

To calibrate the position of each pixel in the real target, we used the data on LED light image through holes on a plate which was placed on the SCIFI block. Figure 9 shows the LED patterns before and after the correction.

To correct the misalignment of the SCIFI sheets, we measured the positions of tracks of 1.6-GeV/c π^+ beam passing through the SCIFI sheets. The mean value of the deviation of a hit position on each SCIFI sheet from the fitted straight-line was ascribed to the misalignment of the SCIFI sheet. Figure 10 shows the misalignment of the sheets before and after the correction. The correction could be made within the accuracy of 100 μm.

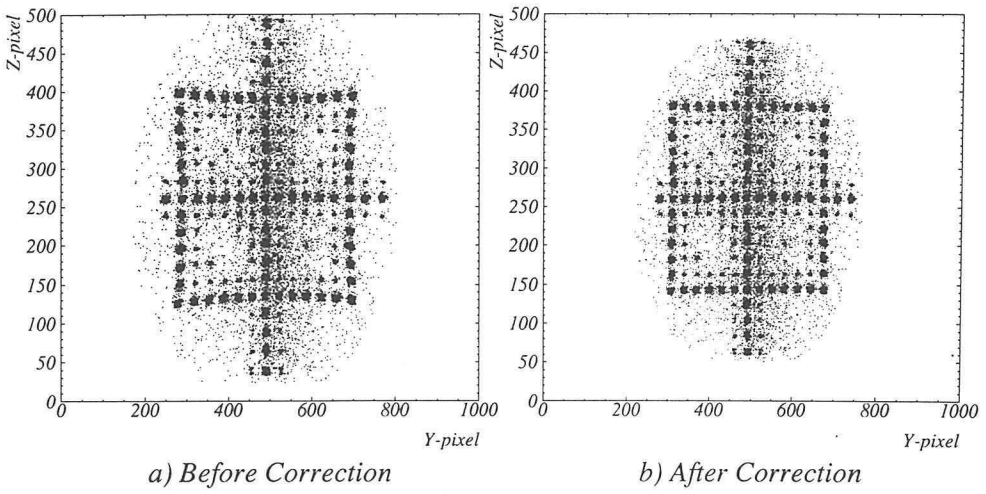

Figure 9: Correction for the LED pattern. Abscissas and ordinates show the pixel-number coordinates.

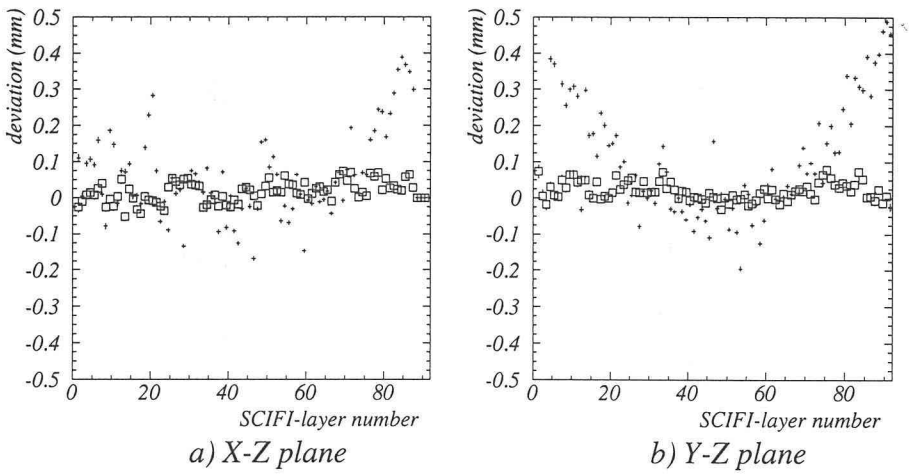

Figure 10: The misalignment of the SCIFI sheet as a function of the SCIFI-layer in the a) X-Z plane and b) Y-Z plane. The crosses show the mean values of the deviation of the center of cluster on each SCIFI sheet from the fitted straight-line. The open squares show the corrected ones.

24.2 Hit Density and Position Resolution of Photo-Electron Image

The clusters of bright pixels for minimum-ionizing tracks were considered to be photo-electron images. Contiguous set of bright pixels were defined as a cluster. The centroid of the brightness was defined as the center of the cluster and was considered to be the position of the photo-electron. The r.m.s. of the brightness distribution around the center was regarded as the size of the cluster. Figure 11 shows the distributions of the cluster sizes perpendicular to the track (Y direction) and along the track (Z direction). The peaks correspond to the sizes of the clusters of single photo-electron, which was about 11 μm on the CCD-chip and 120 μm at the input-window of the I.I.T. The number of photo-electrons for the minimum-ionizing particle was estimated to be about 0.25 /sheet from the number of

clusters.

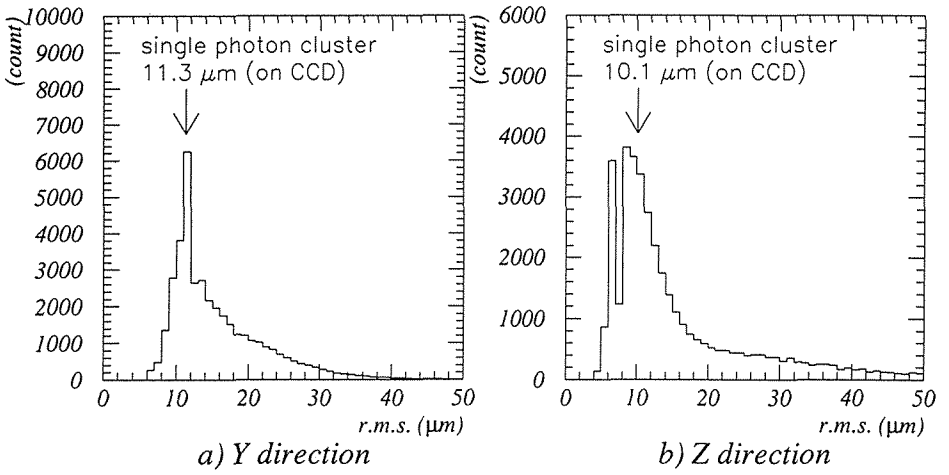

Figure 11: The distributions of the cluster size a) perpendicular to the track and b) along the track.

The distribution of the total brightness in a cluster is shown in Fig. 12. There is no peak corresponding to a single photo-electron because the MCP's on the second and the third stages of the I.I.T. were operated in non-saturated mode.

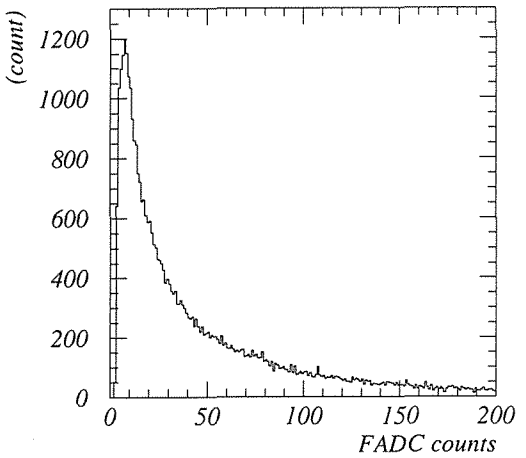

Figure 12: The distribution of the total brightness in a cluster, so called "Harry distribution".

A trajectory in the picture was fitted with a straight line. The distribution of the center of each cluster around the straight line is shown in Fig. 13. The resolution of the SCIFI-target system was found to be 300 μm.

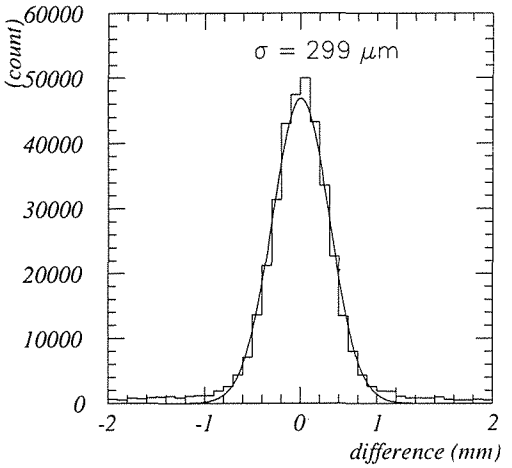

Figure 13: The distribution of the center of the cluster around the fitted straight line. The resolution was evaluated with Gaussian fit to be 300 μm.

2.5 Trigger

The size of image data for the SCIFI-target system was typically 2K pixels per event, and the readout time of the image data was 25 msec as mentioned in Section 2.3.4. Therefore the readout time limited the number of acceptable events. In order to reduce the number of background events, two stages of trigger systems were constructed to select the hyperon production in real-time.

2.5.1 First-Level Trigger

On the first-level trigger, the hyperon production was selected by requiring the (π^+,K^+) reaction, i.e. requiring π^+ for a beam particle and K^+ for a particle in the K^+ spectrometer. The main source of the background was misidentification of π^+ and proton as K^+. Outgoing π^+'s were vetoed by aerogel Čerenkov counters (FAC and SAC), and the momentum region of the outgoing particles was roughly selected by the matrix coincidence signal of CH and FTOF.

The π^+'s in the beam were defined as;

$$\pi_{BEAM} = SPILL \otimes T1 \otimes T2 \otimes BAC \otimes \overline{GC},$$

where $\otimes$ represents "AND" logic. The *SPILL* denotes a spill-gate signal which was made by a timing signal from the accelerator. The $T1 \otimes T2$ stands for a coincidence signal of the TOF counters, the T1 and T2. The *BAC* indicates a signal from BAC which rejected slow particles in the beam, i.e. K^+ and proton. The $\overline{GC}$ is a veto signal from the GC which detected fast particles, i.e. e^+ and μ^+.

The first-level trigger signal was generated by the logics as;

$$\pi_{BEAM} \otimes \overline{BV} \otimes YH \otimes \overline{FAC} \otimes \overline{SAC} \otimes (matrix\text{-}coincidence).$$

The $\overline{BV}$ represents a veto signal from the BV counter. It eliminated events where a π^+

beam did not interact in the SCIFI target or was scattered in a small angle. The *YH* denotes a signal from the YH hodoscope. It was required to reject fake-triggers caused by neutral particles. The *FAC* and *SAC* are veto signals from the two sets of aerogel Čerenkov counters, the FAC and SAC respectively, which were sensitive to π^+'s. The *(matrix-coincidence)* indicates a logic using a matrix coincidence module to select a combination of the hit position on the CH hodoscope and that on the FTOF counters. This logic roughly selected the momentum region of the particles. The selection efficiency as a function of the momentum of the particle is shown in Fig. 14.

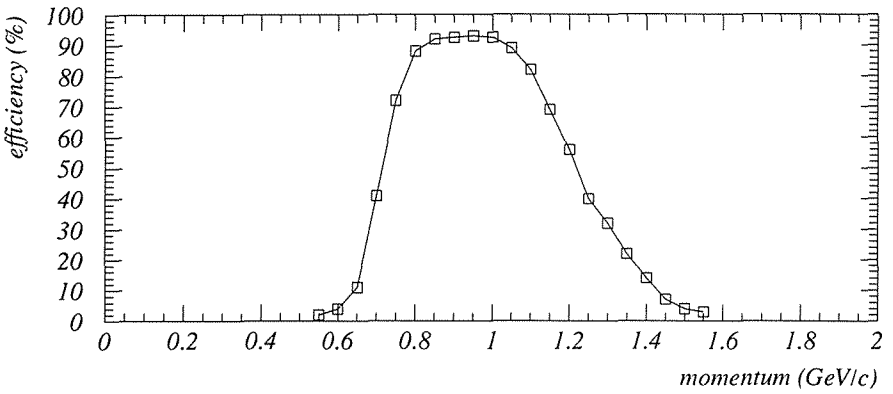

Figure 14: Efficiency of momentum selection with the matrix coincidence.

Typical rate of the first-level trigger signals was 250/spill (125 Hz) for π^+ of 1×10^5 /spill. The dead-time was about 10 %. The first-level trigger was made within 400 nsec and opened the gate of the second-stage image intensifiers.

2.5.2 Second-Level Trigger

The main background in the events selected by the first-level trigger was caused by protons. We eliminated those protons by selecting the mass region of K^+ using the "mass-trigger" logic. For mass selection logic we used the momentum information given by the combination of hit positions on CH and FTOF and the time-of-flight information between T2 and FTOF counters obtained from the fast-encoding TDC modules.

The bending angle of the particle by the SP magnet was obtained from the combination of the hit-counter number of CH and that of FTOF. The TOF information was obtained from the time difference between the T2 and FTOF. We used the fast-encoding TDC system consisting of a TAC (Lecroy TFC) and an ADC (Lecroy FERA-4403B). The TDC had a time resolution of 45 psec and conversion time of 11.2 μsec. The hit-counter number of FTOF and the TOF information were stored in the memory of the FERA module. The hit-counter number of CH was stored in a first-in-first-out (FIFO) memory module (Lecroy data-stack). A sequence of trigger started just after the completion of the conversion of the

TOF in the FERA module. The hit-counter number of FTOF was encoded to a 5-bit code through a programable-logic-unit module (Lecroy PLU). For each hit-counter number of FTOF, the data-stack was cyclically scanned to make a combination with the hit-counter number of CH (4-bit code). The combination was encoded to a 7-bit "momentum"-code according to a table pre-loaded in a memory-lookup-unit module (Lecroy MLU). The 7-bit "momentum"-code was finally compared with the lowest 9 bits of the TDC data using another MLU module which contained 2^{16} bits of trigger-flag data according to the correlation between the TOF and the momentum for K^{+}'s. The sequence continued until all the combinations of the hit counters of CH and that of FTOF were scanned. It took about 100 nsec to investigate one combination of CH and FTOF, and the trigger-flag was generated 14 μsec after the reaction occurred in the SCIFI target. The efficiency of the mass-trigger after the selection by the first-level trigger is shown in Fig. 15 as a function of the mass obtained by the TOF analysis. Typical rate of the second-level trigger was 16/spill (8 Hz)

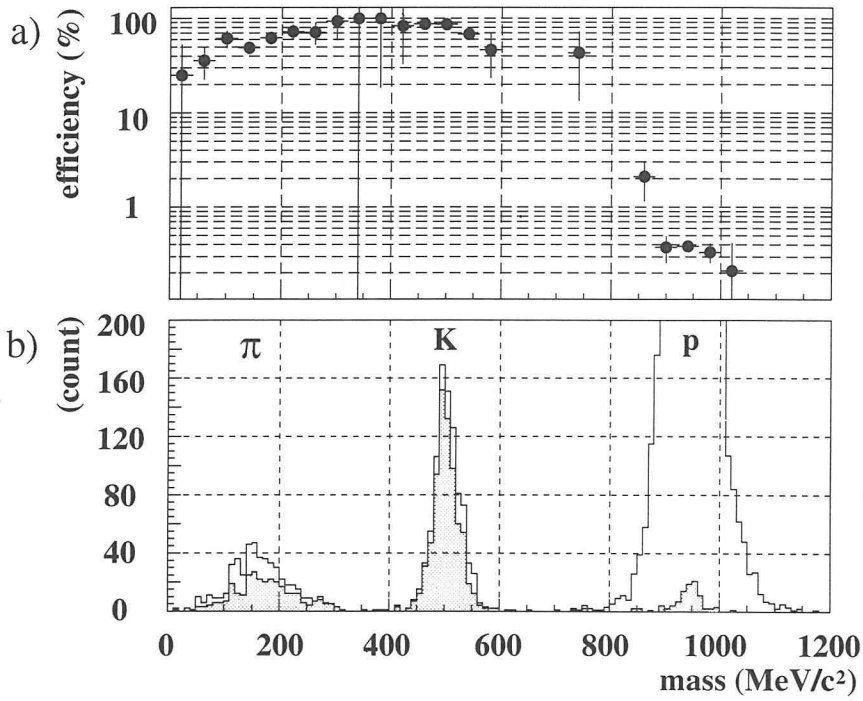

Figure 15: a) The efficiency of the mass-trigger as a function of particle mass. b) The obtained mass spectra with the first-level trigger (area under the solid line) and the second-level trigger (hatched area).

for the π^+ of 1×10^5 /spill. The rate decreased to 12/spill because of the dead-time of the on-line data taking system. The second-level trigger was made within 15 μsec and opened the gate of the third-stage image intensifiers, whereas the holding time of the image in the phosphor at the second stage of the I.I.T. was about 50 μsec.

2.6 On-Line Data Acquisition

The on-line data acquisition system consisted of three independent subsystems. One was for the counters and the chambers, and the other two were for the image data readout of the vertical and the horizontal directions. Each subsystem had a 8-mm tape device on which the collected data were recorded. The correspondence of the three subsystems was insured by putting the common event identification numbers.

2.6.1 Counter Data Acquisition

For the data acquisition for the counters and the chambers a VAX (MicroVAX-2000) with the VMS operating system was used. Signals were digitized with CAMAC and KEK-standard TKO modules [35], and transferred to and stored in the buffer-memory modules in the main CAMAC crate during the beam-on period. The stored data were transferred to a Q-Bus interface (Kinetic 2922) on the VAX through a crate-controller (Kinetic 3922) during the beam-off period. The digitization in the CAMAC and the TKO modules started by the first-level trigger at the rate of 115 Hz. A hardware clear signal suppressed the data transfer to the buffer-memory modules for the events without the second-level trigger.

2.6.2 Image Data Acquisition

For the data acquisition for the SCIFI-target system an on-board VME MC68020 processor with the OS9 operating system was used. The image data were digitized with the image digitizer and stored in the FIFO buffer-memory module as described in Section 2.3.4. The data in the FIFO module was transferred to a VME I/O module whenever the buffer memory was not empty. The free space of the buffer memory was monitored, and when the free space was less than a half of the capacity, the trigger was prohibited to prevent the overflow of the buffer memory.

3 Data Analysis

The SCIFI detector provides visual images in which we can recognize a sequences of the reaction processes, Σ^+ production, Σ^+ scattering and Σ^+ decay. However, most of the produced Σ^+'s decay in flight and only about 0.4 % of the Σ^+'s interact with nuclei in the SCIFI target. The reduction of the data on Σ^+ decays and other background events before scanning by human eyes is vitally important since the maximum number of events which can be scanned by human eyes is limited. In the present experiment the data were selected and analyzed as shown below.

First, beam particles incident on the SCIFI target and outgoing particles from the target were identified. Then, the missing-mass analysis was made for these events. The identification of (π^+,K^+) reactions was essential to select Σ^+ productions, but the data still contained Σ^0 productions and other backgrounds. Secondly, the trajectory of Σ^+ and its decay were recognized by an automatic-tracking program. This process eliminated events with

Σ^0's and Σ^+'s which could not be recognized due to a short flight length before decay, and also other background events. The production angle and the coplanarity of Σ^+ production were checked by the program. In this procedure data reduction was made for starting the scanning procedure by human eyes to select candidates for Σ^+ scattering. Kinematic fitting was then applied to confirm these events. Details are described in the following subsections.

3.1 Counter Data Analysis

3.1.1 Analysis of π^+ Beam

The selection of incident π^+ beam was made with use of TDC data from the T1 and T2 which were corrected for the slewing effect with ADC data. The TOF resolution of about 85 psec was obtained with π^+ beams whose arrival times were spread in ± 1 nsec as shown in Fig.16.

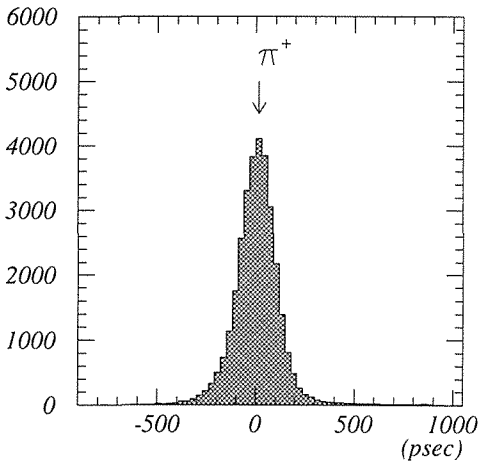

Figure 16: Time-of-flight for incident beam.

The beam momentum was calculated with the transportation matrix of the D2 magnet using the hit information on the BDC1 and BDC2 located upstream of the magnet and that of the BDC3 located downstream of the magnet. If there was no hit on the BDC3, hits on the BPC4 and BPC5 were used taking the transportation matrices of the Q6 and Q7 magnets into account. The tracking efficiency was 99.9 % and the momentum resolution was 0.5 % (r.m.s.). The central value of the π^+ momentum was 1.64 GeV/c and the momentum bite was estimated to be about 0.5 % (r.m.s.).

3.1.2 Analysis of K^+ Measured with the Spectrometer

The outgoing K^+'s were detected with the K^+ spectrometer. Momenta of the charged particles were determined from the hit positions on the CDC, DC1, DC2 and DC3 and the magnetic field of the spectrometer using the spline and the Runge—Kutta method. Flight lengths of the particles were also calculated. Efficiency of the momentum determination for these processes was 88 % and the momentum resolution was 0.9 % (r.m.s.).

Velocities of the particles were calculated from the flight-time and flight length. The

flight-times of the particles from the start counter T2 to the FTOF were obtained by ADC correction for the time slewing effect. By using a mean value of arrival times of photons on the top and bottom photo-tubes, position dependence of the light propagation time through the scintillator slab was compensated. The obtained TOF resolution was about 150 psec. The difference between the arrival times was used for obtaining the vertical hit position on the FTOF counters. The obtained mass spectrum is shown in Fig.17.

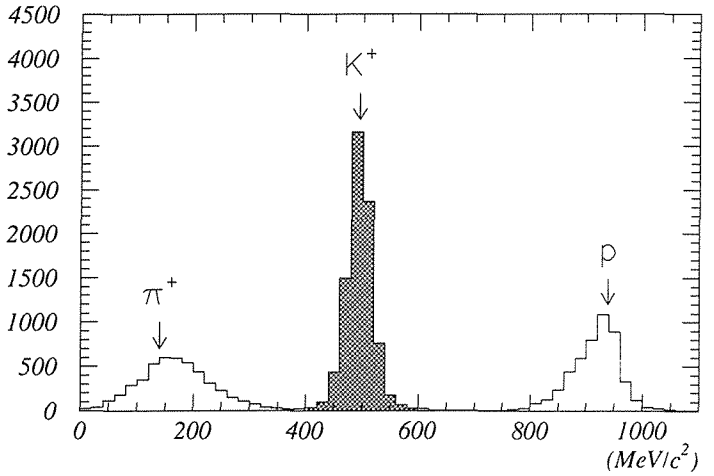

Figure 17: Mass spectrum for outgoing particles. The hatched area was used for the K^+ selection.

The particles in mass region between 400 MeV/c^2 and 600 MeV/c^2 were selected as K^+'s. The accepted momentum region in the trigger was below 1450 MeV/c, where the background contamination was less than 0.4 %.

3.1.3 Selection of Σ^+ production

To select the events of Σ^+ production, the missing masses were calculated from the momenta and the directions of the incident π^+'s and the outgoing K^+'s. Figure 18 shows the missing-mass spectrum. The particles in the region between 1150 MeV/c^2 and 1250 MeV/c^2 was selected for the Σ^+-production candidates. The image data of the SCIFI target for these candidates were analyzed. The trajectories of the tracks measured with the spectrometer were used for the automatic-tracking analysis as shown in Section 3.2.1.

The candidates may contain the reaction $\pi^+ + n \rightarrow K^+ + \Sigma^0$. They were eliminated by the analysis of image data described below by requiring the visible track of Σ^+. The contamination of the events of Λ production were discarded in the same way.

3.2 Image Data Analysis

The next step was the analysis of the image data, in which the recognition of complicated event topologies containing scattering and decay of Σ^+ was indispensable. A conventional way used for the analyses of the data in the bubble chamber was scanning of the trajectories. Since this procedure took a long time, limited number of events could be analyzed.

The present SCIFI detector provided digitized image data which were ready for com-

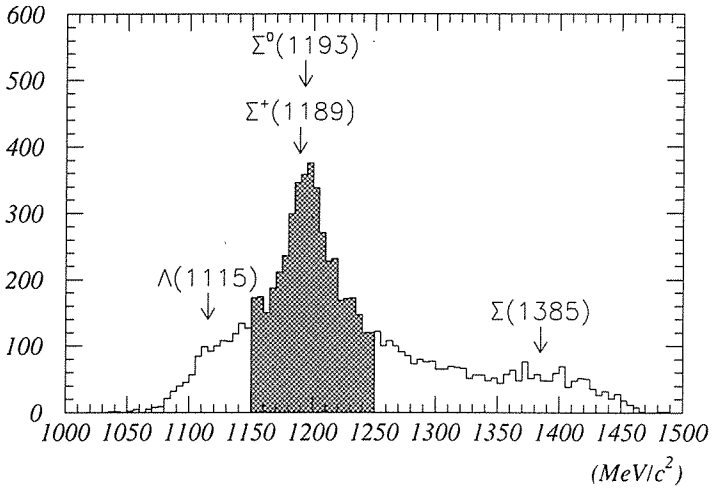

Figure 18: Missing-mass spectrum for (π^+,K^+) events. The hatched area was selected for the Σ^+-production candidates.

puter processing. Therefore, we could introduce a step to discard unnecessary events before the human scanning.

After the data calibration explained in Section 2.4.1, the image data analysis went through the steps of automatic tracking, eye-scanning and kinematic fitting. The efficiencies for all the processes were evaluated with Monte Carlo simulations by feeding simulated image data to the same analysis procedure as the one for the real data.

3.2.1 Automatic Tracking

All the image data of the events which were selected as Σ^+-production candidates in the counter data analysis were fed to the automatic-tracking procedure. The Hough transformation were used for finding the tracks[†].

Hough Transformation The Hough transformation is a projection of a straight line on the y-z plane, that is;

$$y = a\,z + b\,,$$

to the point (a,b) in the a-b plane. Parameters a and b of the straight lines defined by two points in the y-z plane are calculated. If all the points (y,z) are on a straight line, the parameters (a,b) for any two points in the y-z plane are the same.

There are several ways to choose the parameters expressing the line. Instead of the parameters a and b, we adopted ρ for the distance from a fixed point (y_0,z_0) to the straight line, and θ for the angle between the straight line and the Z-axis, as shown in Fig. 19. The points distributing around a line make a cluster in the (ρ,θ) plane. Inversely, if a cluster is found in the (ρ,θ) plane after the transformation, a straight line corresponding to the (ρ,θ) value is recognized. In the present analysis, when θ was positive value, the point at the

[†] The idea to apply the Hough transformation to the analysis of image data for the SCIFI-target system was first suggested by Professor Atsuo Ono of Kobe University.

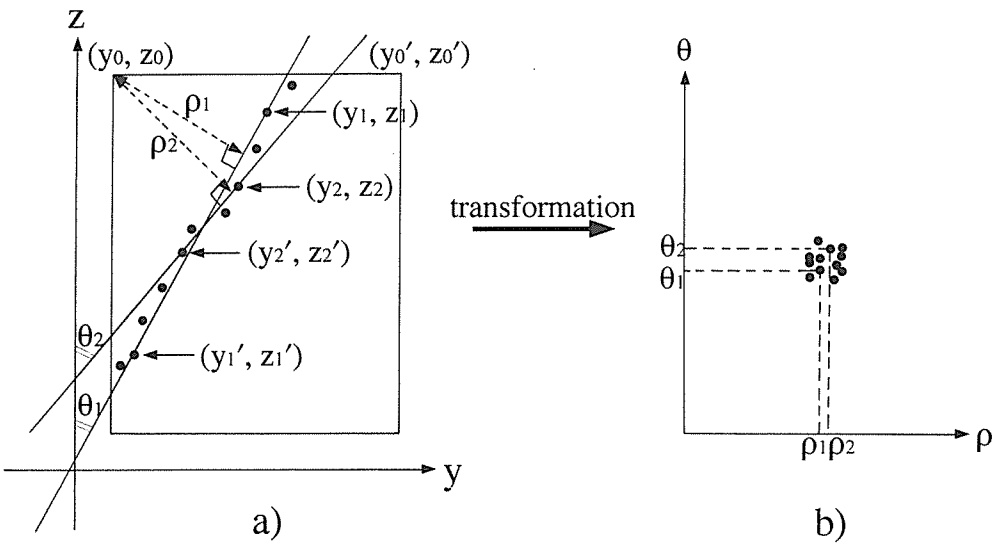

Figure 19: Hough transformation. The points in the (ρ,θ) plane are plotted in b) for all the combinations of two points in the y-z plane in a) (see the text).

corner of the SCIFI target, (y_0,z_0) in Fig. 19 was defined as the fixed point. When θ was negative value, another corner point (y_0',z_0') was used.

The Hough transformation was applied for all the combinations of pixel data of the photon image in the Y-Z and the X-Z planes of the SCIFI target. It was the best way to recognize tracks in the image data because of the following reasons;

- The photon images were observed along a track statistically.
- The event patterns which included the Σ^+ production, and decay or scattering of Σ^+'s had many trajectories to be recognized.
- Dark current of the I.I.T. made random photon spots in the picture.

Event-Pattern Recognition To recognize an event pattern, it was necessary to determine the points of both ends of the track segment and the relation of the tracks. The three-dimensional reconstruction of the tracks was also necessary for the events observed independently in the X-Z plane and the Y-Z plane.

Tracks of the incident π^+ beam, the outgoing K^+, and the Σ^+ emanated from the (π^+,K^+) reaction vertex were searched in a picture. Additionally, we required a branch from the Σ^+ track, which is either a π^+ from Σ^+ decay, a proton from Σ^+ decay, or a proton or a Σ^+ from Σ^+p scattering.

The incident π^+ and outgoing K^+ were minimum ionizing particles which made thin tracks. Σ^+'s made thick tracks due to large energy deposits in the target. The major decay modes of Σ^+ are $p + \pi^0$ (51.57%) and $n + \pi^+$ (48.30%). When the decay particle was a proton, the track was thick, whereas the track of π^+ was thin. When the Σ^+ was scattered in the SCIFI target, both the scattered Σ^+ and the recoil particle made thick tracks.

The detail of the algorithm for the event-pattern recognition is schematically shown in Fig. 20 and is explained below.

1. Applying the brightness cut on the pixel data, only bright spots were left. A thick track which consisted of bright spots was found with the Hough transformation.

The energy deposit was large enough to make clusters contiguously along the track. The segment was then recognized as a straight line which consisted of the bright points. The track parameters were determined by linear fitting of the points belonging to the segment. The points recognized as a member of the segment were removed from the data list and the process was repeated until further significant cluster was not found by the Hough transformation.

2. After removing thick segments, incident and outgoing tracks were found with a help of information from the beam line and the spectrometer. Points in the upstream region of the target which formed a line parallel to the external beam track were found and regarded as the incident track inside the target. The outgoing track inside the target was found by the same way in the downstream region with the external information. The tracks recognized to be the ones due to the incident and outgoing particles were also removed from the data.

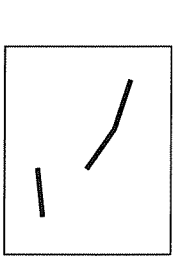

1. Thick segments are found by the Hough transformation.

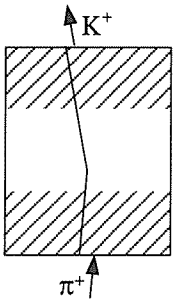

2. Incoming and outgoing tracks are found with a help of external tracks.

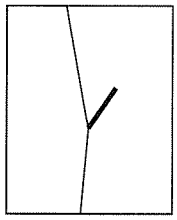

3. A thick segment emanated from the crossing point of incoming and outgoing tracks is found.

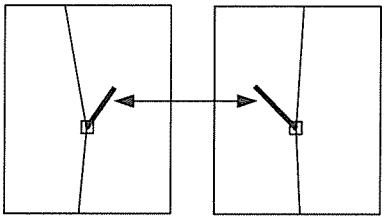

4. Vertex point is calculated on each plane. If the Z-positions of the vertices on both planes are close each other, the thick segment is regarded as a candidate for a Σ^+ produced at the vertex point.

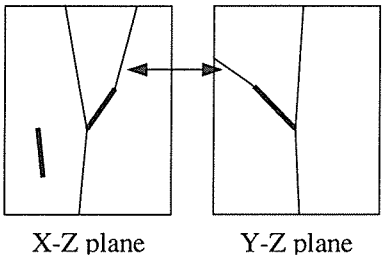

5. A branch from the track of Σ^+ candidate is searched by means of the Hough transformation. When the segments of the branch on the both planes are consistent each other, the event is regarded as a candidate for decay or scattering of Σ^+.

Figure 20: Outline of the event-pattern recognition algorithm.

3. Among the thick segments found in item 1., the tracks which intersected with the incoming and outgoing tracks were selected.
4. Above processes were carried out independently for the X-Z plane and Y-Z plane. A vertex position was calculated for each plane with incoming and outgoing tracks and one of the thick segments. For any combinations of the thick segments in the both planes, the vertex positions on the X-Z plane and the Y-Z plane were compared. If the difference of Z-positions of the vertex on both planes were within 1 cm, the thick segment was regarded as a candidate for a produced Σ^+.
5. For each candidate of the produced Σ^+ track found above, a branch from the track was searched for. There were two ways to find it.
   (a) We picked up a branch obtained in item 1.
   (b) For the remained points, we applied the Hough transformation again with a lower threshold value of the brightness. In order to find a branch from Σ^+ segments, we required that one of two points to calculate (ρ,θ) was the one belonged to the Σ^+ segments. This requirement restricted the search only for the straight line intersecting to the Σ^+ segments.

   If the segments of the track of the branch on the both planes were consistent each other, the event was regarded as a candidate for decay or scattering of Σ^+.

An example of typical event of the Σ^+ production and decay which was recognized by the above algorithm is shown in Fig. 21.

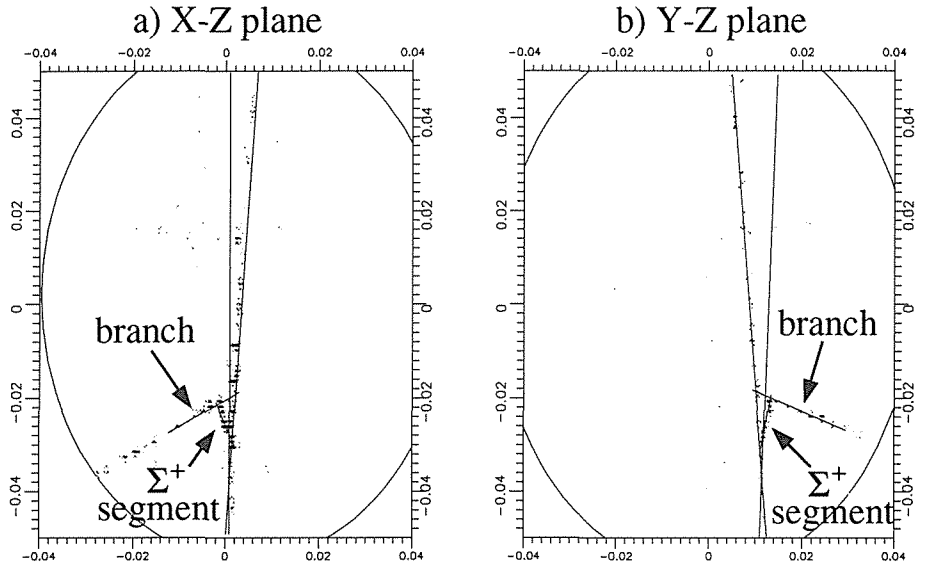

Figure 21: An example of the result of the automatic-tracking process for the real image data. The images on the a) X-Z plane and b) Y-Z plane are shown.

The resolution and the efficiency of this automatic-tracking program were evaluated by applying the program to simulated image data as described in Section 3.3. The differences between the position obtained by the program and the generated position of the simulation data are shown in Fig. 22 for the positions of production and decay. The tails in the distributions were considered as a misidentification of the process. The position resolutions were evaluated for the peaks. The resolutions of the production position were 1.20 mm, 0.27

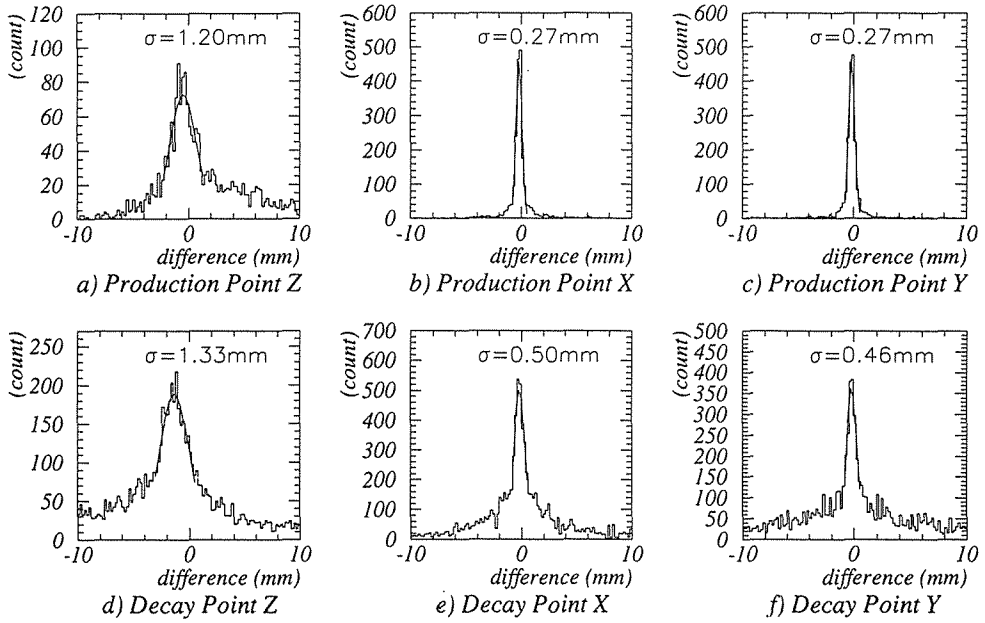

Figure 22: The differences between the position obtained by the automatic-tracking process and the generated position of the simulation data. The differences in the production positions are shown for a) Z-direction, b) X-direction and c) Y-direction. The differences in the decay positions are shown for d) Z-direction, e) X-direction and f) Y-direction.

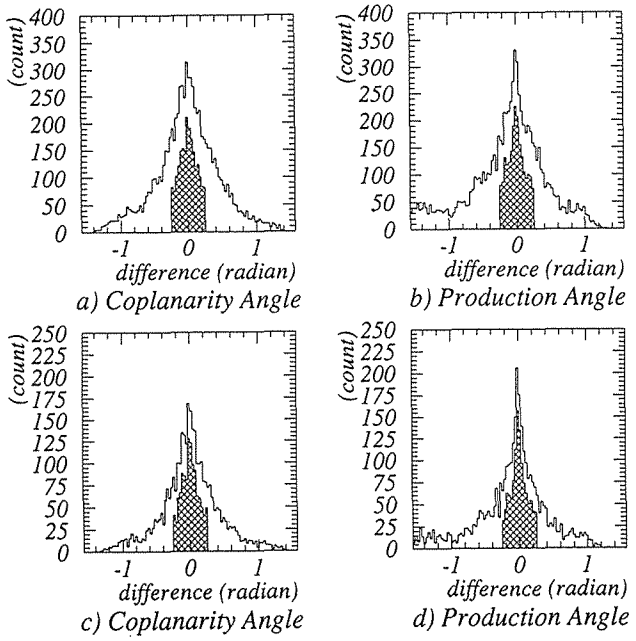

Figure 23: The deviations from the coplanarity conditions and the deviations of the production angles from the one predicted by the kinematics for the real image data. The deviations are shown for all the tracks a) in the coplanarity angle and b) in the production angle, and for the tracks longer than 1 cm c) in the coplanarity angle and d) in the production angle. The hatched areas show events which satisfied the kinematic requirements in the automatic-tracking process as explained in the text.

mm and 0.27 mm for the X direction, Y direction and Z direction respectively. The resolutions of the decay position were 1.33 mm, 0.50 mm and 0.46 mm for the X direction, Y direction and Z direction respectively.

The angular deviation of Σ^+ tracks were obtained from the generated direction of the simulated data. The angular resolution of the direction of Σ^+ track was evaluated to be 0.11 radian. For the tracks longer than 1 cm, the resolution was 0.05 radian.

By applying the kinematics of the reaction $p(\pi^+,K^+)\Sigma^+$ on the tracks of π^+, K^+ and Σ^+ tracks, the requirements for the coplanarity and production angles were;

- the deviation from the coplanarity condition is within $\pm$0.25 radian,
- the deviation of the production angle from the one predicted by the kinematics is $\pm$0.25 radian.

The results of the requirements were shown as hatched area in Fig. 23. With these additional requirements, we obtained the background reduction of 80% in the automatic-tracking process. The efficiencies of the automatic-tracking program evaluated by simulated image data were about 47 % for events of Σ^+ production on the hydrogen and about 64 % for events of Σ^+p scattering. If the flight length of Σ^+ was more than 1 cm, the efficiencies were 80 % for events of Σ^+ production and 90 % for events of Σ^+p scattering in the simulation.

3.2.2 Eye-Scanning

Events of 6×10^4 were selected in the automatic-tracking process. Human operators scanned the selected image data and categorized the event patterns in detail, and then put marks on the points of interest. Pointing of the marks was carried out with a "mouse" on the graphic display. We call this process "eye-scanning". The aim of this process was to confirm the Σ^+-production events and to pick up Σ^+p scattering events.

All the events were classified into six categories. Information on the brightness of the track, such as "thick" or "thin", was not considered in the classification. Figure 24 shows schematic pictures of all the categories.

Type-RK: The track of Σ^+ candidate associated with a recoil prong which is followed by a "kink" as shown in Fig. 24 a). This is regarded as a candidate for Σ^+p scattering followed by decay of the scattered Σ^+ particle.

Type-KK: The track of Σ^+ candidate with two "kinks" subsequently as shown in Fig. 24 b). This is a candidate for Σ^+ scattering where a recoil track is very short or neutral. Scattering of a decay particle of the Σ^+ in the target is also categorized as this pattern.

Type-R: The track similar to the type-RK but without "kink" as shown in Fig. 24 c). This is a candidate of Σ^+ scattering with decay outside the fiducial area. If the flight length of Σ^+ after scattering is too short to be identified or the decay angle is too small, the event is categorized as this pattern.

Type-K: The track of Σ^+ candidate with a "kink" as shown in Fig. 24 d). This is a candidate of the Σ^+ production followed by decay.

Type-V: "V"-shape topology separated from the (π^+,K^+) vertex as shown in Fig. 24 e). This is regarded as a candidate for decay of a Λ particle. This type of events is misidentified as a Σ^+ candidate in automatic tracking if the decay point is close to a track of π^+ or K^+.

Type-N: Other patterns are categorized into this type. One of them is an event in which there is neither Σ^+ candidate track nor "V"-shape topology as shown in Fig.24 f). This is a candidate of a Λ production in which the Λ decays outside the fiducial area. Another one is an event with "Y"-shape topology, which has a track of Σ^+ candidate without "kink" nor recoil prong. This is a candidate of the Σ^+ production in which the decay product is not visible due to the same reason as in the case of type-R.

For the events classified into other categories than type-N, the reaction point, kink point and the end point of each track were recorded.

For calculation of the Σ^+p scattering cross section, the number of Σ^+-production events and the number of Σ^+p scattering events were evaluated. The number of Σ^+-production events was calculated from the number of K-type events corrected by the efficiencies of the analysis procedures. The number of Σ^+p scatterings was evaluated from the number of the RK-type events. The events classified into other categories were not used in further analysis.

The following four data sets were randomly mixed in eye-scanning.

1. Real image data which were selected by automatic tracking.
2. Real image data without selection by automatic tracking.

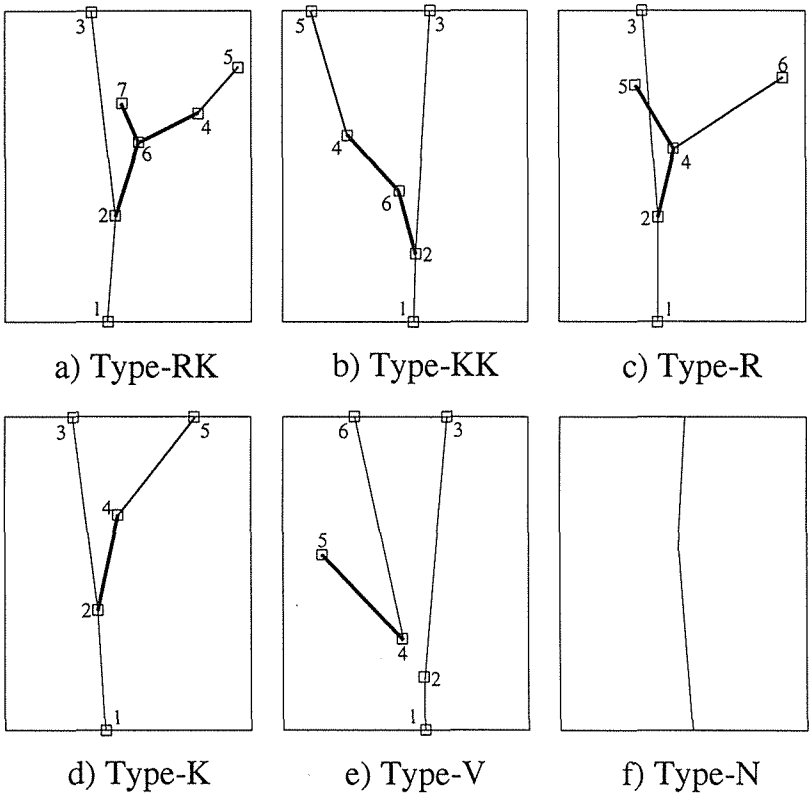

Figure 24: The categorization by eye-scanning. The open squares and the numbers in the pictures indicate the recorded points and the pointing order in eye-scanning process respectively (see the text). For type-N, no pointing was done.

3. Simulated image data of Σ^+ production.
4. Simulated image data of Σ^+p scattering.

Data Sets 3. and 4. were generated by the Monte Carlo simulation described in Section 3.3, and used to find the efficiency and to confirm the reliability of eye-scanning. The efficiency of automatic tracking for the real image data were evaluated from Data Set 2. (see Section 3.3.2).

The results of the classification by eye-scanning are summarized on Table 6.

Category	RK	KK	K	R	V	N	Total
1)	415	4991	32141	982	5154	14146	57829
2)	20	213	1640	49	699	3697	6318
3)	34	310	2575	83	13	1905	4920
4)	3568	605	3019	3575	123	2468	13358

1) Real image data with automatic tracking.
2) Real image data without automatic tracking.
3) Simulated image data of Σ^+ production.
4) Simulated image data of Σ^+p scattering.

Table 6: Number of events for each category classified by eye-scanning.

The position resolution for pointing the marks with the mouse was evaluated with the simulated image data. Figure 25 shows the angular resolution of the Σ^+ track as a function of the flight length. The resolution was inversely proportional to the flight length and the coefficient was about 0.79 mm. It means that the position resolution in the perpendicular direction to the track was 0.79 mm. Figure 26 shows the resolution of the flight length

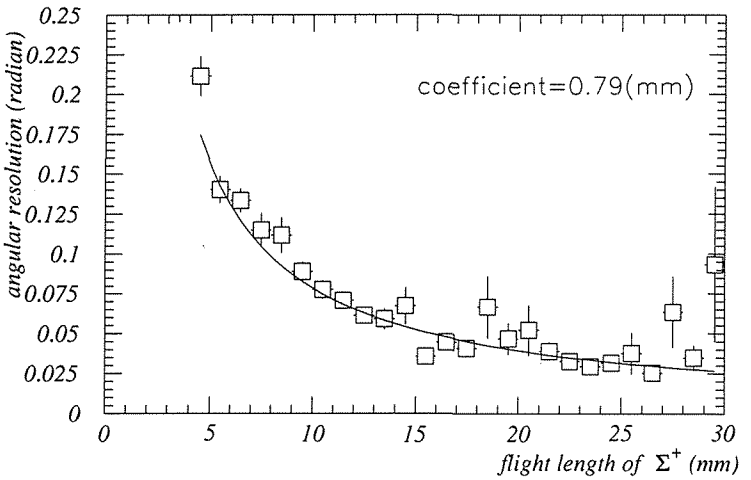

Figure 25: The angular resolution of the Σ^+ track as a function of the flight length evaluated with the simulation data. The solid line shows the result of fitting with inversely proportional function. The coefficient of 0.79 mm shows the position resolution in the perpendicular direction to the track for pointing the marks with the mouse.

which corresponds to the position resolution in the track direction of about 1.2 mm. These resolutions are used in the kinematic fitting in Section 3.2.5.

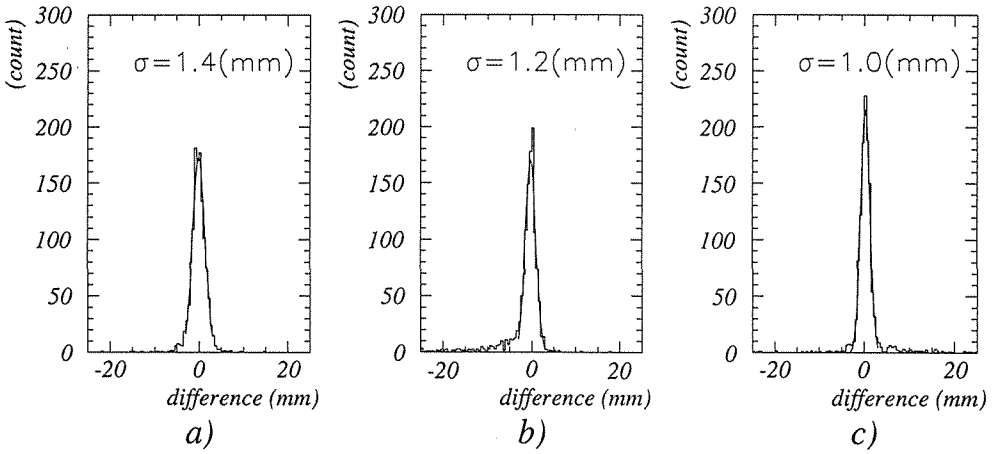

Figure 26: The differences in the track directions between the positions obtained by eye pointing and the generated positions of the simulation data. The differences are shown for a) Σ^+ track before scattering, b) Σ^+ track after scattering and c) recoil proton tracks. The resolutions for pointing were evaluated with Gaussian fit to be a) 1.4 mm, b) 1.2 mm and c) 1.0 mm respectively. The solid lines show the results of the fitting.

3.2.3 Visibility Requirement

If the visible flight length is short or the angle between the tracks is small, the categorization of the event is ambiguous. Track visibility was required to minimize the ambiguity.

The K-type events selected in eye-scanning process contained Σ^+ production on a hydrogen and that on a carbon nucleus without scattering. We applied the visibility cut whose parameters were tuned by simulation study. The remained events were tested with the kinematic fitting procedure described in Section 3.2.5. When a track was confirmed as a Σ^+ produced on a hydrogen by kinematic fitting, we called it an H-like event. The Σ^+ momentum was determined kinematically from momenta of the incident π^+ and the outgoing K^+ and the direction of Σ^+. Other tracks were considered as Σ^+'s produced on carbon nuclei. We called them C-like events. The C-like events were also used in the analysis, if the Σ^+ decayed to a proton and π^0 and then the decay proton stopped in the fiducial area. In this case a Σ^+ momentum could be obtained kinematically using the kinetic energy of proton deduced from the range-energy relation. To solve the decay kinematics, severer conditions for visibility on the flight length of the decay particle were required.

The procedure was applied for K-type events and RK-type events categorized by eye-scanning. The RK-type events contained Σ^+p scattering. The cut parameters used are summarized below.

1. Requirements for an H-like K-type event
   (a) Minimum flight length
      i. Length of Σ^+ track is longer than 6 mm.
      ii. Length of decay track is longer than 3 mm.

(b) Minimum angle
i. Decay angle is larger than 0.2 radian.
(c) Minimum distance
i. Distance from decay point to outgoing K^+ track is longer than 1 mm.
(d) Minimum position difference in the Z direction between the starting point and the end point of the track
i. Difference for Σ^+ track is larger than 1 mm.

2. Requirements for a C-like K-type event
(a) Minimum flight length
i. Length of Σ^+ track is longer than 6 mm.
ii. Length of decay track is longer than 6 mm. The decay track is required to be stopped in the fiducial area.
(b) Minimum angle
i. Decay angle is larger than 0.2 radian.
(c) Minimum distance
i. Distance from decay point to outgoing K^+ track is longer than 1 mm.
(d) Minimum position difference in the Z direction between the starting point and the end point of the track
i. Difference for Σ^+ track is larger than 1 mm.
ii. Difference for decay track is larger than 1 mm.

3. Requirements for a RK-type event
(a) Minimum flight length
i. Length of Σ^+ track before scattering is longer than 4 mm.
ii. Length of Σ^+ track after scattering is longer than 4 mm.
iii. Length of recoil proton track is longer than 3 mm. The recoil track is required to be stopped in the fiducial area.
(b) Minimum angle
i. Decay angle is larger than 0.1 radian.
(c) Minimum distance
i. Distance from decay point to recoil proton track is longer than 1 mm.
ii. Distance from decay point to Σ^+ track before scattering is longer than 1 mm.
iii. Distance from scattering point to outgoing K^+ track is longer than 1 mm.
iv. Distance from end point of recoil proton track to Σ^+ track after scattering is longer than 1 mm.
v. Distance from production point to Σ^+ track after scattering is longer than 1 mm.
(d) Minimum position difference in the Z direction between the starting point and the end point of the track
i. Difference for Σ^+ track before scattering is larger than 1 mm.
ii. Difference for Σ^+ track after scattering is larger than 1 mm.
iii. Difference for recoil proton track is larger than 1 mm.

The most important cut parameter is the one applied to the flight length of Σ^+. It was desirable to set the cut parameters for the flight lengths as short as possible, because the flight length of Σ^+'s is very short ($c\tau = 2.396$ cm). Figure 27 a) shows the combined efficiency of automatic tracking and eye-scanning for the K-type events as a function of flight

length of Σ^+. The values were obtained from the simulated Σ^+-production data. The efficiency for Σ^+ with the flight length of 6-mm was about 20 %. The value increased to 40 % for Σ^+ with the flight length of 1 cm. The limitation was due to other visibility conditions. Besides the efficiency the eye pointing procedure could cause a systematic error in the flight-length determination. Figure 27 b) shows differences between the flight length obtained by eye pointing and the generated one. We used a cut parameter of 6 mm for the flight length, with which the systematic error for the length determination was less than 1 mm.

Other important cut parameters are related to decay particles. We chose 3 mm for the cut parameter of flight length of a decay particle in the case of H-like events and 6 mm in the case of C-like events. Furthermore, the distance between the decay point and the outgoing K^+ track was required to be more than 1 mm in order to avoid the overlap of tracks. The position difference in the Z direction between the starting point and the end point of Σ^+ was required to be more than 1 mm because a track perpendicular to the Z direction showed a broken-line due to the alternating layer structure.

The analysis of Σ^+p scattering was performed for the events categorized as RK-type in eye-scanning. The cut parameters of the flight length for a Σ^+ track before scattering, a Σ^+ track after scattering and a recoil proton track were 4 mm, 4 mm and 3 mm respectively, in which the systematic errors for the length determination were about 1 mm. The scattering kinematics was solved for both the H-like events and the C-like events without using the

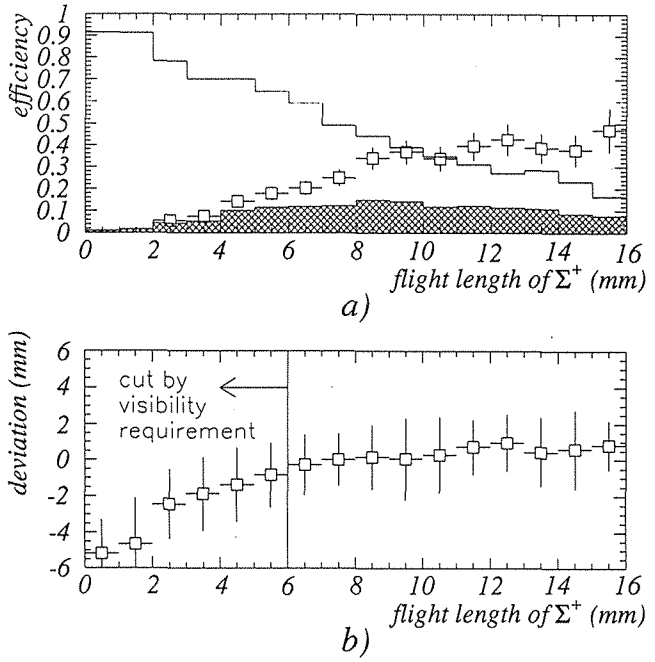

Figure 27: a) The combined efficiency of automatic tracking and eye-scanning for the K-type events as a function of the flight length of Σ^+ is shown as the open squares. It is obtained from the simulated Σ^+-production data. The upper histogram is the flight length distribution of produced Σ^+'s. The lower histogram with hatched area shows the number of survived events after automatic tracking and eye-scanning. b) The difference between the flight length of Σ^+ obtained by eye pointing and the generated one.

track of decay particle of Σ^+.

In addition to the visibility requirements, the fiducial area was defined as an area surrounded by an ellipse which had a long axis of 9 cm in the beam direction and a short axis of 7 cm both for the X-Z and the Y-Z plane. All the points necessary for the analysis were required to be in the area. For H-like events points of production and decay of Σ^+'s were required to be in the fiducial area. For C-like events the decay protons were required to stop in the fiducial area additionally. The identification of Σ^+ scattering required the recoil proton track to stop in the fiducial area. The stopped points on the X-Z and Y-Z planes were required to be consistent each other within two layers of the SCIFI sheet.

The efficiency of event selection by the visibility requirement was evaluated with use of simulation data. The details are described in Section 4.1.

3.24 Brightness Requirement

The brightness of trajectories was examined for thick tracks, i.e. Σ^+ tracks and proton tracks. Since energy deposits of the Σ^+ and the proton were large, their tracks were relatively thick.

The required thresholds were;

- sum of the brightness for X-Z and Y-Z planes corresponds to the counts more than 250/mm in FADC.
- sum of the brightness for each plane corresponds to the counts more than 100/mm in FADC.

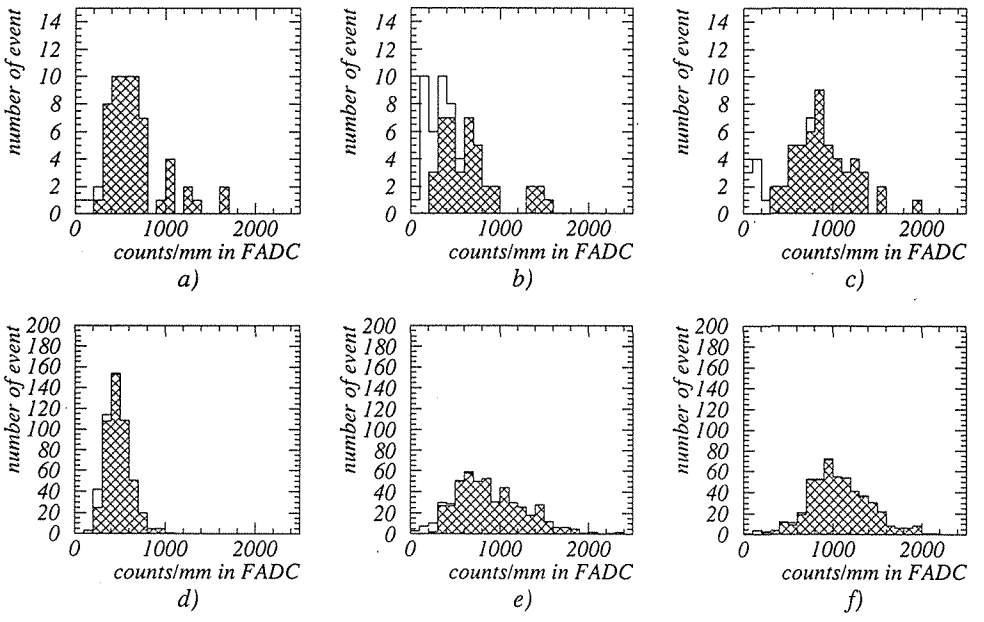

Figure 28: The event distributions for average brightness. The average brightness is expressed as the sum of the counts per mm in FADC. The distributions in the real data are shown for a) Σ^+ track before scattering, b) Σ^+ track after scattering, and c) recoil proton track. The distributions in the simulation data are shown for d) Σ^+ track before scattering, e) Σ^+ track after scattering, and f) recoil proton track. The hatched areas correspond to the events which survived the brightness cut.

Figure 28 shows the distributions of average brightness for Σ^+ tracks before and after scattering and those for recoil proton track for the Σ^+p scattering candidates. The hatched areas correspond to the events which survived the brightness cut. Efficiencies for this requirement were better than 95 % in all the cases. The distributions for the real data and the simulation data show good agreements.

3.2.5 Kinematic Fitting

The candidates for Σ^+-production events were categorized into H-like events (Σ^+ production on a hydrogen) and C-like events (Σ^+ production on a carbon) by checking whether the observed variables satisfy the kinematics of Σ^+ production on a hydrogen. The kinematic constraints are expressed by the following equations of the energy—momentum conservations;

$$
\begin{aligned}
C_1 &= p_\pi \sin\theta_\pi \cos\phi_\pi - p_K \sin\theta_K \cos\phi_K - p_\Sigma \sin\theta_\Sigma \cos\phi_\Sigma , \\
C_2 &= p_\pi \sin\theta_\pi \sin\phi_\pi - p_K \sin\theta_K \sin\phi_K - p_\Sigma \sin\theta_\Sigma \sin\phi_\Sigma , \\
C_3 &= p_\pi \cos\theta_\pi - p_K \cos\theta_K - p_\Sigma \cos\theta_\Sigma , \\
C_4 &= E_\pi + m_p - E_K - E_\Sigma , \\
C_5 &= E_\pi{}^2 - p_\pi{}^2 - m_\pi{}^2 , \\
C_6 &= E_K{}^2 - p_K{}^2 - m_K{}^2 , \\
C_7 &= E_\Sigma{}^2 - p_\Sigma{}^2 - m_\Sigma{}^2 ,
\end{aligned}
$$

where ten observed variables, o_i ($i = 1,\cdots,10$), are;

$$E_\pi, E_K, p_\pi, p_K, \theta_\pi, \theta_K, \theta_\Sigma, \phi_\pi, \phi_K \text{ and } \phi_\Sigma,$$

and two unobserved variables, u_k ($k = 1,2$), are;

$$E_\Sigma \text{ and } p_\Sigma .$$

E_π, E_K and E_Σ are energies and p_π, p_K and p_Σ are momenta of the incident π^+, outgoing K^+ and produced Σ^+ respectively. The θ's and ϕ's are dip angles and azimuthal angles for the tracks indicated by the subscripts respectively. The masses of the particles are denoted as m_π, m_K and m_Σ. The energies and momenta of π^+ and K^+ were obtained by the analysis of spectrometer data.

Kinematic fitting is a method to obtain the best fit within the kinematic constraints. The constraints C_j's ($j = 1,\cdots,7$) should be zero to satisfy the kinematics in the ideal case. The C_j's, however, do not satisfy the kinematics in the real experimental data since the observed variables have experimental errors. The functions to be minimized is given as;

$$S = G_{il}\, a_i\, a_l ,$$

where a_i's are;

$$a_i = o_i - f_i .$$

The f_i's (i =1,$\cdots$,10) are the parameters to fit the observed variables o_i. The G_{il} is an inverse error matrix of the observed variables, in which the resolutions for pointing the marks and the momentum resolutions for incident π^+ and outgoing K^+ were included. The position resolution for pointing the marks in the perpendicular direction to the track was 0.79 mm, and that in the track direction was 1.2 mm. The momentum resolution for π^+ was 0.5 %, and that for K^+ was 0.9 %. The f_i's should satisfy C_j's to be zero within experimental errors.

The minimization of S under the constraints on C's was performed with the Lagrange multiplier method [36]. With additional Lagrange multipliers λ_j (j = 1,$\cdots$,7), S is replaced by;

$$S + 2\lambda_j C_j ,$$

and the minimization condition is given as;

$$\frac{1}{2}\frac{\partial S}{\partial a_i} + \lambda_j \frac{\partial C_j}{\partial a_i} = 0 .$$

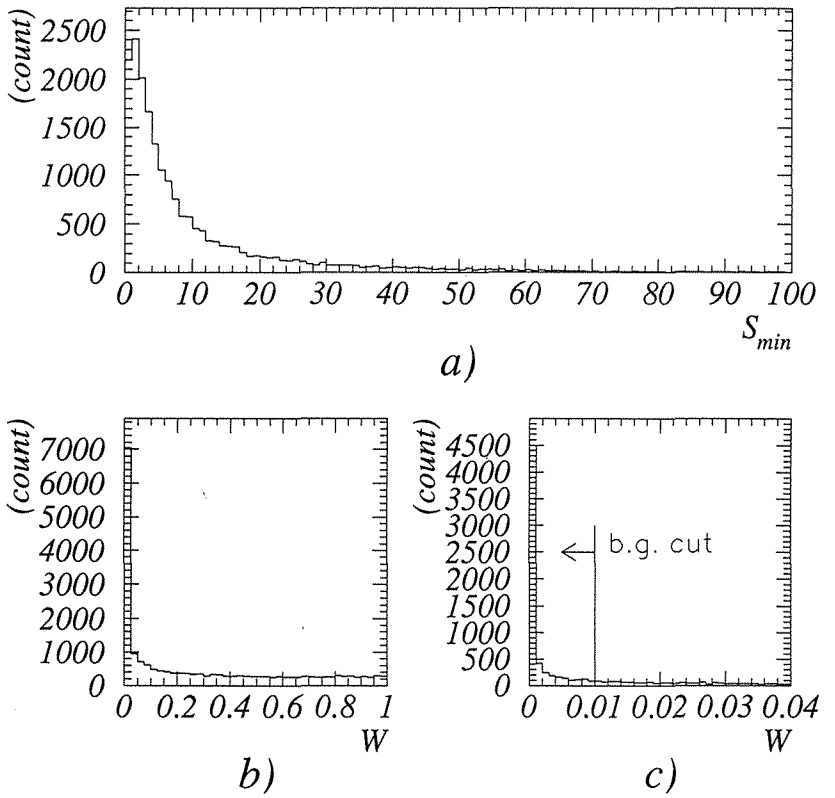

Figure 29: Results of the kinematic fitting assuming that the Σ^+ is produced on a hydrogen. a) The event distribution for the minimized S. b) The event distribution for the upper tail probability W (see the text). c) An expanded figure of a part of b) in which the event distribution with different binning in the lower region of W are shown. The b.g. cut means the cut of background events with W below 0.01.

Since the constraints had non-linear terms, the minimization was performed with successive iteration. The results of the fitting were checked by the χ^2 test. Since the measurement had two over-constraint variables, the distribution of the minimized S, that is S_{min}, obeyed the χ^2-distribution with the degrees of freedom of two. Considering the upper tail probability of the χ^2-distribution;

$$W(\chi^2) = \int_{\chi^2}^{\infty} f(u)\, du ,$$

where $f(u)$ is the χ^2-distribution, the $W(\chi^2)$ distributes uniformly between 0 and 1. Since the distribution of the S_{min} included events which did not satisfy the kinematics, the distribution of the $W(S_{min})$ has a peak around zero as shown in Fig. 29. The background events with $W(S_{min})$ below 0.01 were cut, whereas 99 % events of the Σ^+ production on a hydrogen nucleus were retained after this cut.

The events which were cut by kinematic fitting were regarded as C-like events and were analyzed with severe requirements for visibility described before. The Σ^+ was required to decay to a proton and a π^0, and the decay proton was required to stop in the fiducial area. As the energy and momentum of the proton were obtained from the range-energy relation, the kinematics of the event could be obtained completely.

The resolution of the determined variables were evaluated with use of the simulated image data described in Section 3.3. Figure 30 shows the momentum resolutions for the

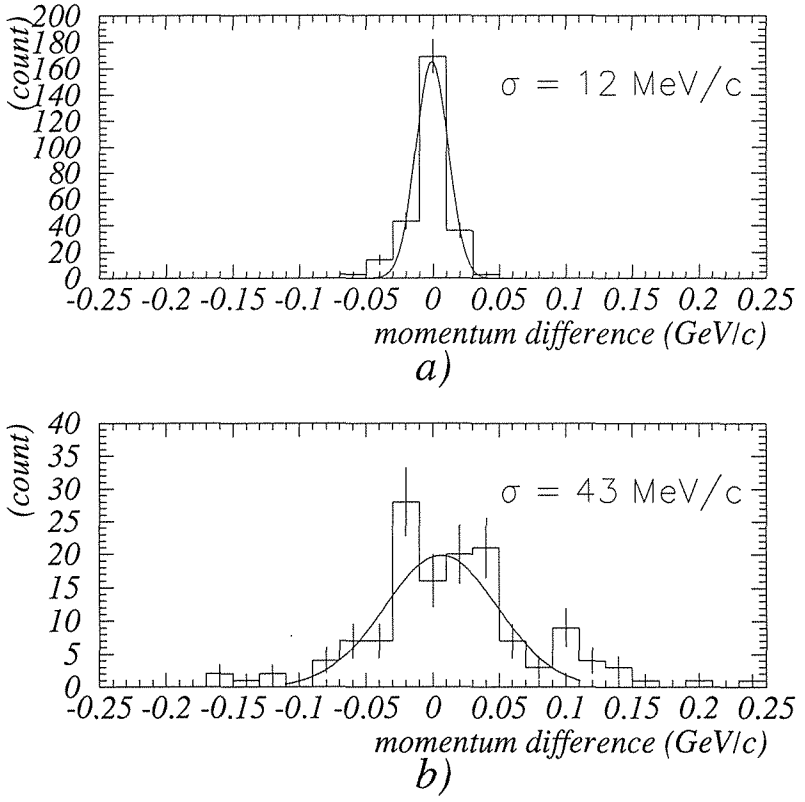

Figure 30: a) The differences between the momenta of Σ^+'s obtained by the kinematic fitting with the simulation data and generated ones in the case of the hydrogen target. The resolution of the Σ^+ momentum was found to be approximately 12 MeV/c. b) The momentum differences in the

produced Σ^+'s. The obtained momenta were compared with the generated ones. We obtained the momentum resolution of approximately 12 MeV/c for the simulated image data in the case of hydrogen target and that of approximately 43 MeV/c for the ones in the case of carbon target. The resolution was worse in the carbon case than in the hydrogen case because the resolution of decay angle was limited.

If Σ^+'s produced on carbon nuclei were misidentified as H-like events, the momentum resolution obtained for a H-like event by kinematic fitting should be worse than the one for real H-like events. The resolution was evaluated by kinematic fitting with use of the simulated image data in the case that Σ^+'s were produced on carbon nuclei and were misidentified as H-like events. The obtained resolution was approximately 53 MeV/c.

The kinematic fitting was performed for the candidates of the Σ^+p scattering events to confirm the Σ^+ scattering kinematics in the case of a hydrogen target and to eliminate the scattering on carbon nuclei. The events were classified to the following two cases and examined with the appropriate kinematic constraints.

a) The Σ^+ produced on a hydrogen is scattered on a hydrogen.

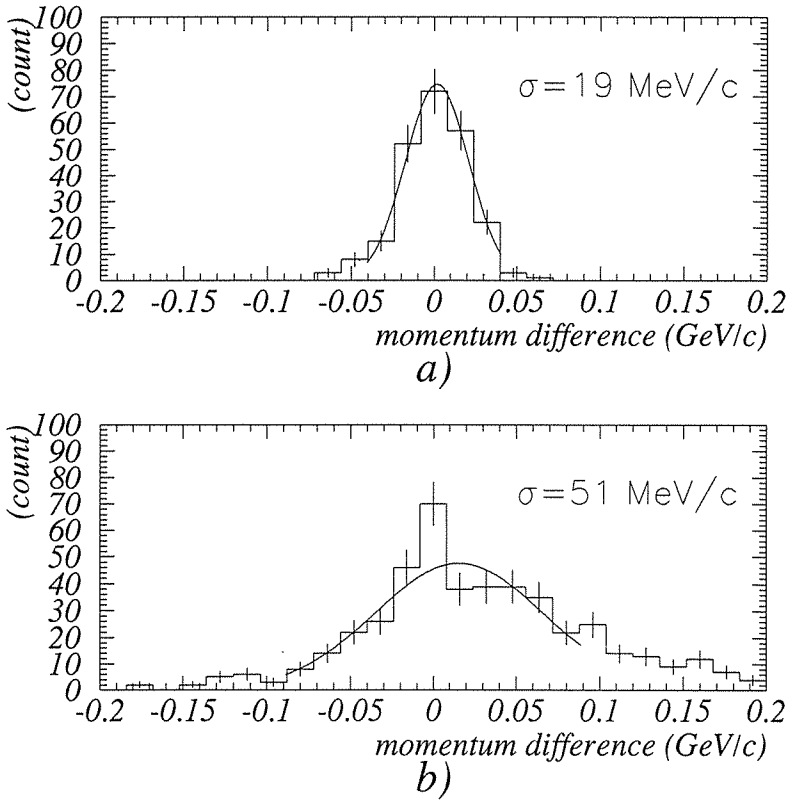

Figure 31: The differences between the momenta of Σ^+'s just before the scattering obtained by the kinematic fitting with the simulation data and generated ones. a) The momentum differences for the events in which the Σ^+'s were produced on hydrogens and scattered on hydrogens. The resolution of the Σ^+ momentum was found to be approximately 19 MeV/c. b) The momentum differences for the events in which the Σ^+'s were produced on carbon nuclei and scattered on hydrogens. The resolution was approximately 51 MeV/c.

b) The Σ^+ produced on a carbon is scattered on a hydrogen.
The kinematic constraints for Σ^+p scattering are given as;

$$
\begin{aligned}
C_1 &= p_{\Sigma_i}\sin\theta_{\Sigma_i}\cos\phi_{\Sigma_i} - p_{\Sigma_f}\sin\theta_{\Sigma_f}\cos\phi_{\Sigma_f} - p_p\sin\theta_p\cos\phi_p ,\\
C_2 &= p_{\Sigma_i}\sin\theta_{\Sigma_i}\sin\phi_{\Sigma_i} - p_{\Sigma_f}\sin\theta_{\Sigma_f}\sin\phi_{\Sigma_f} - p_p\sin\theta_p\sin\phi_p ,\\
C_3 &= p_{\Sigma_i}\cos\theta_{\Sigma_i} - p_{\Sigma_f}\cos\theta_{\Sigma_f} - p_p\cos\theta_p ,\\
C_4 &= E_{\Sigma_i} + m_p - E_{\Sigma_f} - E_p ,\\
C_5 &= E_{\Sigma_i}^2 - p_{\Sigma_i}^2 - m_\Sigma^2 ,\\
C_6 &= E_{\Sigma_f}^2 - p_{\Sigma_f}^2 - m_\Sigma^2 ,\\
C_7 &= E_p^2 - p_p^2 - m_p^2 ,
\end{aligned}
$$

where E's, p's, θ's and ϕ's are energies, momenta, dip angles and azimuthal angles respectively. The subscripts Σ_i, Σ_f and p represent Σ^+ before scattering, Σ^+ after scattering and

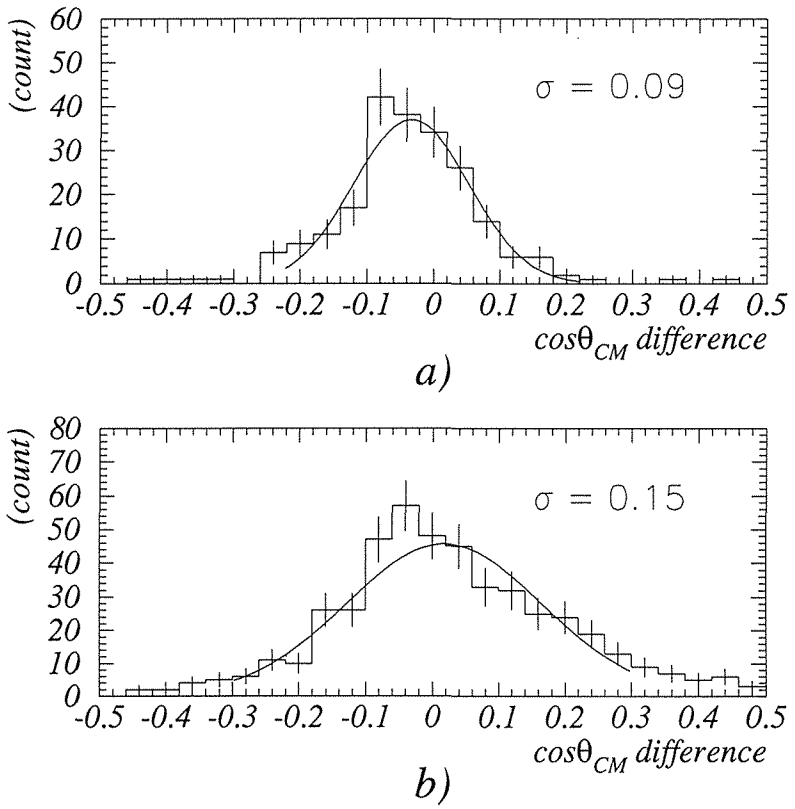

Figure 32: The differences between $\cos\theta_{CM}$ obtained by the kinematic fitting with the simulation data and generated ones. a) The differences for the events in which the Σ^+'s were produced on hydrogens and scattered on hydrogens. The resolution of $\cos\theta_{CM}$ was found to be approximately 0.09. b) The differences for the events in which the Σ^+'s were produced on carbon nuclei and scattered on hydrogens. The resolution was approximately 0.15.

recoil proton respectively.

The minimized S_{min} obeys the χ^2-distribution if the effect of background is negligible. Two possibilities exist. a) There were three over-constraint variables, and the degrees of freedom for the χ^2-distribution was three. b) There were two over-constraint variables, and the degrees of freedom was two.

Figure 31 shows the momentum resolutions of the outputs of the kinematic fitting obtained from the simulation data analysis. They were evaluated by comparing the results of the kinematic fitting for the simulated image data with the generated ones. In the case of a) in which produced momenta of the Σ^+'s were given by the spectrometer analysis, the obtained resolution was approximately 19 MeV/c as shown in Fig. 31 a). In the case of b) in which produced momenta of the Σ^+'s were not given, the resolution was approximately 51 MeV/c as shown in Fig. 31 b).

The scattering angle in the C.M. system, θ_{CM}, was also obtained by the kinematic fitting. Figure 32 shows the resolution of $\cos\theta_{CM}$. The obtained resolution was approximately 0.09 in the case of a), and it was approximately 0.15 in the case of b).

In Table 7 the number of events which survived each analysis process are summarized.

	Experimental Data			Simulation Data		
Eye-Scanning	type-K		type-RK	type-K		type-RK
	32141		415	913		1343
	H	C		H	C	
Visibility Requirement	23496	5892	62	669	188	525
Brightness Requirement	22304	4886	33	649	154	468
Kinematic Fitting	13703	2006	11	356	62	377

Table 7: The number of events which survived each analysis process. "H" means H-like Σ^+-production events and "C" means C-like events.

3.3 Image Data Simulation

In this section, we describe the method to produce simulation data and evaluate the validity of the method.

3.3.1 Production of Simulation Data

The Monte Carlo simulation to produce dummy image data was performed using the GEANT 3.15 package [37]. Two kinds of dummy image data were generated, one for Σ^+ production and the other for Σ^+ production followed by scattering on a hydrogen. The steps to generate the dummy image are shown below.

1. The incident momentum of π^+ beam was set to 1.64 GeV/c with the momentum spread of 14 MeV/c (standard deviation).
2. Σ^+ productions in the reactions $p(\pi^+,K^+)\Sigma^+$ and $C(\pi^+,K^+)\Sigma^+$ were simulated. The cross section and angular distribution of the reaction $p(\pi^+,K^+)\Sigma^+$ shown in reference [38] were used for the purpose. In the case of reaction $C(\pi^+,K^+)\Sigma^+$, we simulated the quasi-free Σ^+ production in the π^+ p reaction where the proton has a Fermi motion in

a carbon nucleus. The momentum distribution of proton is given as;

$$N(p) = \frac{N_0}{1 + \exp\left(\dfrac{p(\mathrm{GeV}/c) - 0.1}{0.05}\right)}.$$

3. The energy loss of the particle in each SCIFI sheet obtained with GEANT was converted to the photons in scintillating fiber.
4. The generated photons were uniformly distributed in scintillating fiber (500 μm $\times$ 500 μm) on the I.I.T. surface. The positions of photons were spread out additionally by 200 μm because of the misalignment of the SCIFI stack and the position resolution of the I.I.T. system. The data could be reproduced with the assumption that the number of photo-electrons on the photo-cathode of I.I.T. obeys the Poisson distribution with the average number of electrons of six per MeV. The amplification of photo-electrons in the I.I.T. was adjusted to have the total brightness counts in FADC of about 55$\pm$15 per photo-electron. The photons were distributed on the CCD pixels with the Gaussian distribution whose width was 250 μm.

3.3.2 Comparison of the Simulation Data with the Real Data

Width of Track and Brightness First, basic properties of trajectories of the image data

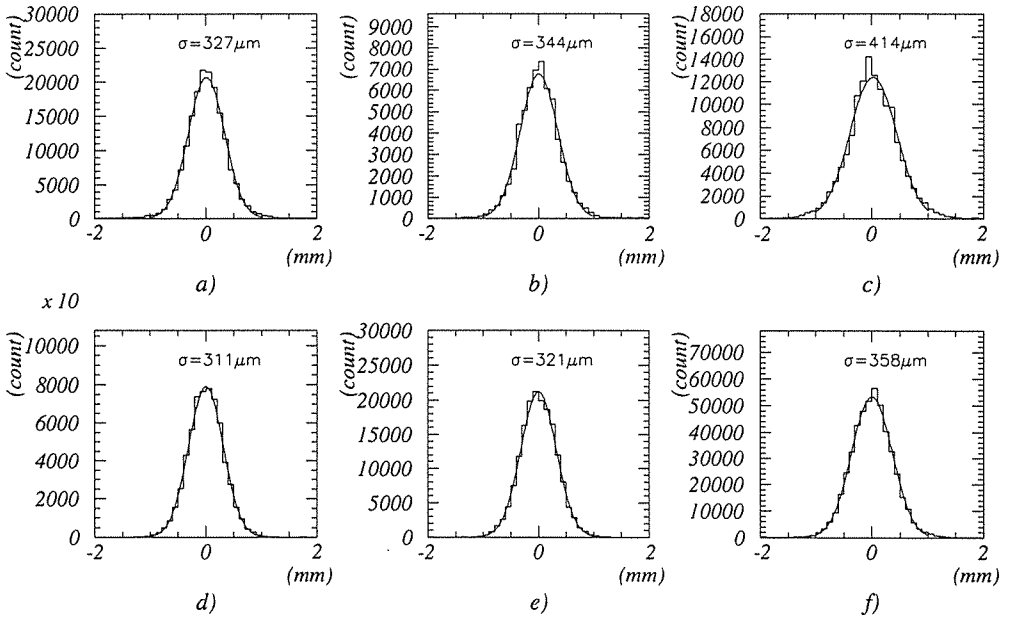

Figure 33: The projections of the brightness distributions on the axes perpendicular to the direction of tracks. The distributions in the real data are shown for a) π^+ track, b) K^+ track and c) Σ^+ track. The distributions in the simulation data are shown for d) π^+ track, e) K^+ track and f) Σ^+ track. The widths of tracks were evaluated with Gaussian fit to be a) 327 μm, b) 344 μm, c) 414 μm, d) 311 μm, e) 321 μm and f) 358 μm respectively. The solid lines show the results of fitting.

produced by the simulation were compared with those of the real data.

Using the K-type events, tracks of π^+, K^+ and Σ^+ were recognized with information obtained by means of pointing by human eye, and then the tracks were fitted by straight lines using the centroid of the brightness of pixel. The width of track was obtained from the projection of the brightness distribution on the axis perpendicular to the direction of tracks. Figure 33 shows the results of the simulation and real data. The widths in the simulation for the π^+ and K^+ are in good agreement with those of real data. The width for the simulated Σ^+ track is smaller than that for the real data by 20 %. This difference was found to be negligible in the evaluation of the efficiencies for the automatic-tracking program as described later.

The average brightness per millimeter for tracks was also compared as shown in Fig. 34. The average brightness distribution for the real data agreed well with those for the simulation data. The efficiency of the brightness requirement (see Section 3.2.4) for the Σ^+ track in the simulation is also in good agreement with those for the real data.

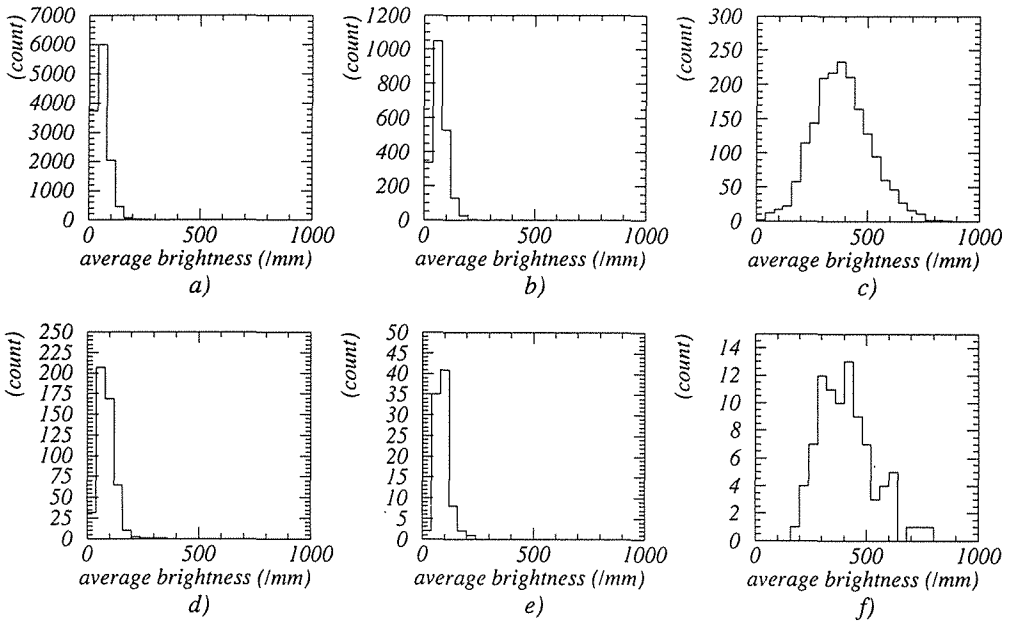

Figure 34: The average brightnesses per millimeter in the real data are shown for a) π^+ track, b) K^+ track and c) Σ^+ track. Those in the simulation data are shown for d) π^+ track, e) K^+ track and f) Σ^+ track.

Comparison by Means of the Automatic-Tracking Program One of the crucial tests for validity of simulation data is the examination of results obtained by means of the automatic-tracking program. Random admixture of the simulation data and the real data without automatic tracking were used for carrying out eye-scanning as described in 3.2.2. For selecting Σ^+ production in the data, the events were required to be categorized as type-K and regarded as the reaction $\pi^+ + p \rightarrow K^+ + \Sigma^+$ by the kinematic fitting. The selected data have been processed by the automatic-tracking program and the efficiencies of the process for both data set as a function of the Σ^+ flight length were compared. The results are

shown in Fig. 35 demonstrating that the both efficiencies agree well.

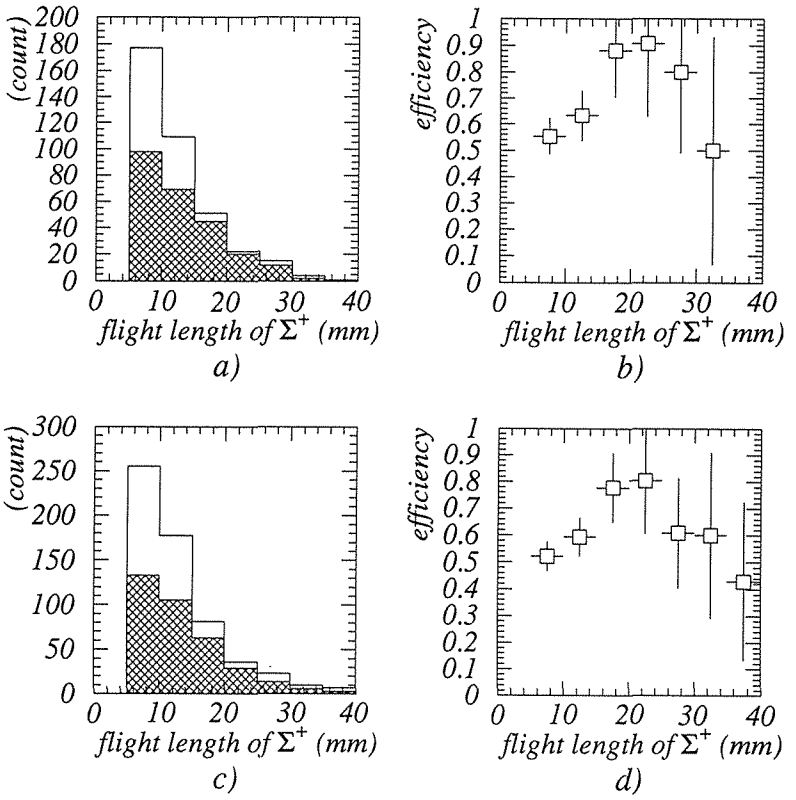

Figure 35: The efficiencies of the automatic-tracking program for the real data and the simulation data. a) The event distribution for flight length of produced Σ^+'s for the real data. The hatched area shows the survived events after automatic tracking. b) The efficiency of the automatic tracking for the real data. c) The event distribution for flight length of produced Σ^+'s for the simulation data. The hatched area shows the survived events after automatic tracking. d) The efficiency of the automatic tracking for the simulation data.

Life-Time of Σ^+ A test of the efficiency correction was performed also by reproducing the life-time of Σ^+ in the data.

The mean flight length, $\hat{x}$, of the particle with the life-time τ is given as;

$$\hat{x} = c\tau \cdot \beta\gamma = c\tau \cdot \frac{p}{m},$$

where m, p are the mass and the momentum of the particle, respectively. If p is constant, the number of events as a function of the flight length x can be deduced with the decay constant $-\hat{x}$. For charged particles in material $\frac{m}{p} \cdot x$ is replaced by L which is defined as;

$$L = \int_0^x \frac{m}{p(\xi)} \cdot d\xi ,$$

taking the energy losses of the particle into account.

The decay rates as a function of L before and after the correction were evaluated in the

region of L between 1 cm and 8 cm as shown in Fig. 36. The decay constant was calculated with the logarithmic likelihood method. The result was;

$$c\tau = 2.38 \pm 0.24 \text{ cm},$$

which agrees with known value [39];

$$c\tau = 2.396 \pm 0.012 \text{ cm}.$$

It should be noted that the efficiency corrections applied here includes those for all the processes to evaluate the cross section, i.e. efficiencies for the automatic tracking, the eye-scanning, the brightness requirement and the kinematic fitting.

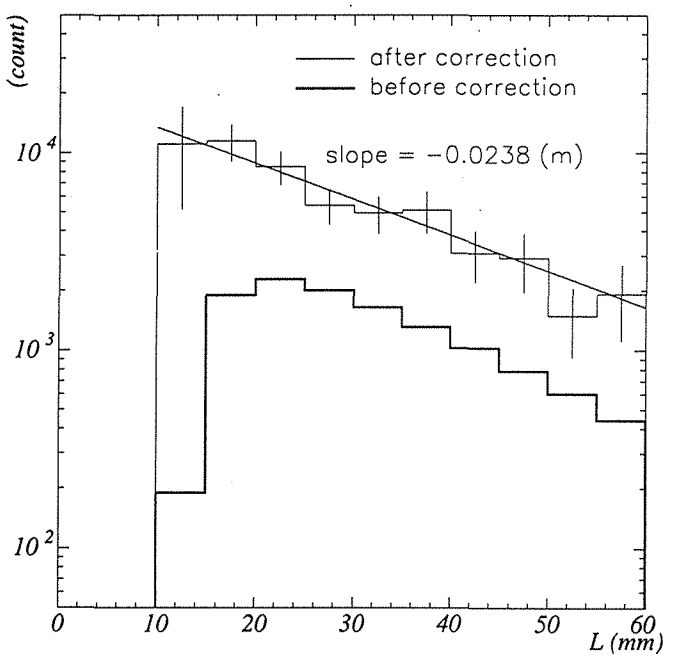

Figure 36: The event distribution for L which is defined with the flight length and the momentum (see the text) before and after the efficiency correction. The decay constant was calculated with the logarithmic likelihood method for the distribution after the correction in the region of L between 1 cm and 8 cm. The $c\tau$ was obtained to be 2.38 ± 0.24 cm.

4 Derivation of the Cross Section and Evaluation of the Errors

We derived the cross section for Σ^+p elastic scattering from the experimental data by the following procedure. The Σ^+'s whose flight length were longer than the threshold value, L_{thr}, was used as incident particles for scattering, where the flight length was defined as the length from the production point to the decay point of Σ^+. In this analysis L_{thr} was 4 mm. The thickness of the target depends upon the flight length of each Σ^+, that is L_i. Therefore,

for calculation of the cross section it is convenient to define the effective number of Σ^+'s, N_{Σ^+}, as the sum of the number of real Σ^+'s weighted by the factor proportional to ($L_i - L_{thr}$) of each Σ^+ in the SCIFI target. The effective number of Σ^+'s is given as;

$$N_{\Sigma^+} = \sum_{i=1}^{n_{\Sigma^+}} \frac{L_i - L_{thr}}{\Delta l},$$

where n_{Σ^+} was the number of produced Σ^+'s and Δl was considered to be the "unit thickness of the target" that was 0.1 mm, whose sum corresponds to ($L_i - L_{thr}$). With use of N_{Σ^+} and the observed number of Σ^+p scatterings, N_{scat}, the cross section for scattering was calculated by the formula;

$$\sigma = \frac{N_{scat} / \varepsilon_{scat}}{N_{\Sigma^+} / \varepsilon_{\Sigma^+}} \frac{1}{\rho \Delta l},$$

where ρ is number density of hydrogen nuclei in the SCIFI target, $\rho = 4.78 \times 10^{22}$ (/cm^3), and ε_{Σ^+} and ε_{scat} are the efficiencies of the analyses for the Σ^+ production and Σ^+p scattering, respectively.

We made estimates of the correction factors including the efficiencies, ε_{Σ^+} and ε_{scat}, for momentum bins of 300 – 400 MeV/c, 400 – 500 MeV/c and 500 – 600 MeV/c and also for hydrogen-like (H-like) and carbon-like (C-like) Σ^+-production events separately. The numbers, N_{Σ^+} and N_{scat}, were obtained for each bin. The cross section was derived by summing up the numbers corrected by the efficiencies. The events of Σ^+p scattering were divided into two regions of scattering angle in the center-of-mass system, that is $-0.4 \leq \cos\theta_{CM} < 0.1$ and $0.1 \leq \cos\theta_{CM} < 0.6$. The differential cross section, $d\sigma / d\Omega$, were obtained for both angular regions.

We evaluated two kinds of correction factors for both ε_{Σ^+} and ε_{scat}, namely, an efficiency related to the kinematics of the event and an efficiency related to the pattern recognition. The efficiency related to the kinematics includes the visibility requirements and the fiducial cuts. This efficiency corresponds to a kinematic effect and was evaluated by simulation of the kinematics of the reaction and the energy loss of the particles in the SCIFI target. The pattern recognition efficiency includes the efficiencies for automatic tracking, eye-scanning, brightness requirement and also for kinematic fitting. This efficiency was evaluated by using the simulated image data processed through the analysis. The correction factors were given by the multiplication of both efficiencies.

4.1 Efficiency Correction

Table 8 summarizes the efficiencies and the corrected values of effective number of Σ^+'s per Δl (0.1 mm) in the three different momentum regions. The actual numbers of Σ^+'s are shown on the last line in Table 7 which were used to obtain errors of the effective numbers of Σ^+'s and the efficiencies. The results of the corrected values of effective numbers of Σ^+'s have an error of about 10 %, which mainly come from the limited number of the simulation data.

The number of the events which were finally identified as Σ^+p scattering was 11. The

Momentum (MeV/c)	300 – 400		400 – 500		500 – 600	
Production Target	H	C	H	C	H	C
Efficiency ε_{Σ^+} (Statistical Error)	.202 (±.032)	.047 (±.017)	.216 (±.019)	.023 (±.007)	.226 (±.052)	.017 (±.006)
N_{Σ^+} ($\times 10^5$) (Statistical Error)	2.85 (±0.05)	0.52 (±0.02)	8.45 (±0.09)	0.67 (±0.03)	1.88 (±0.04)	0.34 (±0.02)
$N_{\Sigma^+}/\varepsilon_{\Sigma^+}$ ($\times 10^6$) (Statistical Error)	1.41 (±0.23)	1.09 (±0.39)	3.91 (±0.35)	2.87 (±0.95)	0.83 (±0.19)	2.04 (±0.69)
Sum of H and C ($\times 10^6$) (Statistical Error)	2.50 (±0.45)		6.78 (±1.01)		2.87 (±0.72)	
Sum of All ($\times 10^7$) (Statistical Error)			1.22 (±0.13)			

Table 8: Efficiency corrections for effective number of Σ^+'s per 0.1 mm. "H" in production target means H-like Σ^+-production events and "C" means C-like events. N_{Σ^+} denotes the effective number of Σ^+'s. Sums of H-like events and C-like events are shown for each momentum bin and for all the momentum bins.

production targets, flight lengths of Σ^+ before and after scattering and recoil proton, momenta at the scattering points and the scattering angles in the center-of-mass system for these events are listed in Table 9. The pictures of a typical event in the SCIFI target are shown in Fig. 37.

Run-Spill-event	Production Target	Σ^+ Before Scattering (mm)	Σ^+ After Scattering (mm)	Recoil Proton (mm)	Momentum (MeV/c)	Scattering Angle $\cos\theta_{CM}$
430-3143-01	C	17.0	4.4	7.8	352	-0.116
449-2894-12	C	5.2	35.8	34.8	506	0.066
451-0503-04	C	11.2	6.5	6.0	413	0.246
462-3343-07	C	10.7	8.5	7.6	430	0.214
465-1484-12	H	13.2	4.3	8.2	415	0.176
506-2907-03	C	26.5	6.6	21.4	477	-0.072
517-2799-07	C	12.6	7.4	4.0	314	0.112
533-2304-02	C	6.0	15.5	6.6	448	0.364
539-0819-03	H	4.5	18.9	9.0	419	0.131
555-1674-03	C	21.7	5.7	5.0	468	0.555
569-0567-13	H	6.3	4.4	4.1	475	0.545

Table 9: List of Σ^+p scattering events. "H" in production target means H-like Σ^+-production events and "C" means C-like events.

The correction factors for the number of Σ^+p scatterings were obtained by the similar way as those for the effective number of Σ^+'s. In addition to the estimation of the number of produced Σ^+'s, the efficiencies for identification of the recoil proton track were taken into account. In Fig. 38 two kinds of the efficiencies are given as a function of scattering angle in the center-of-mass system. The present experiment covered the angular region, $-0.4 \leq \cos\theta_{CM} < 0.6$.

Table 10 summarizes the efficiencies and the corrected values of Σ^+p scattering for the

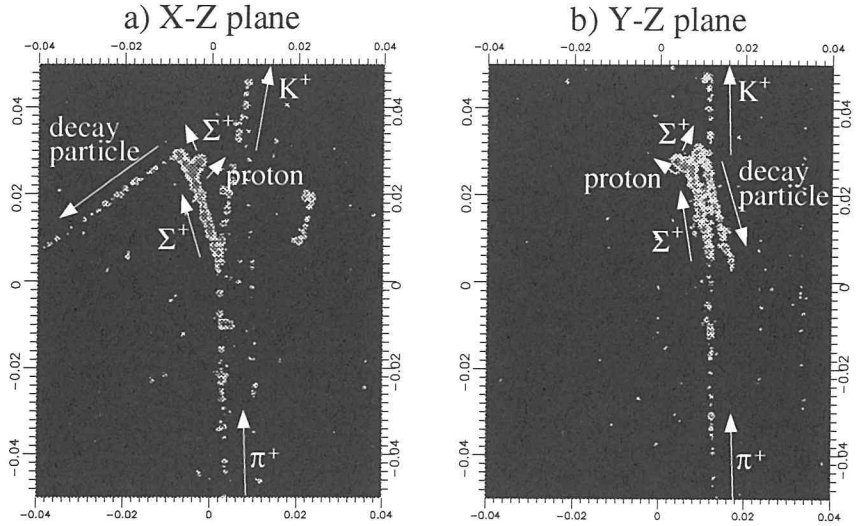

Figure 37: The pictures of a typical event finally identified as Σ^+p scattering. The images on the a) X-Z plane and b) Y-Z plane are shown.

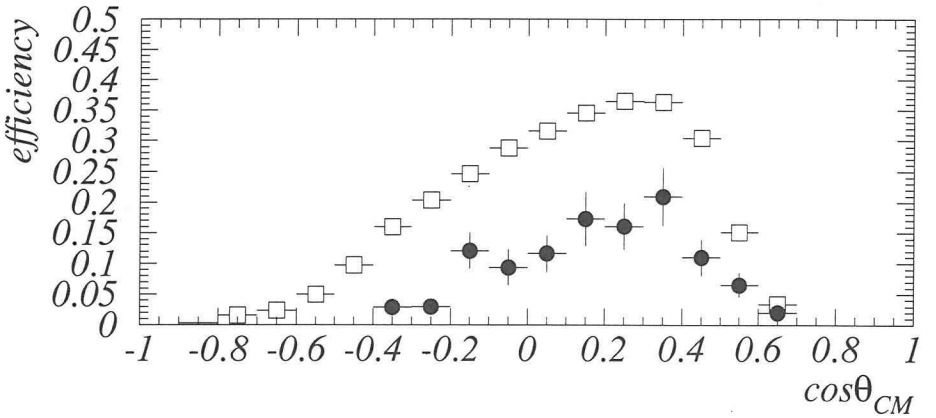

Figure 38: The efficiencies of the analysis for Σ^+p scattering as a function of scattering angle in the center-of-mass system. The open squares show the efficiency for the visibility requirement and the fiducial cut only. The closed circles show the total efficiency.

three momentum regions and the two regions of scattering angle in the center-of-mass system. Errors shown in the table include the statistical ones for the data and the ambiguities of efficiency determination due to the limited number of simulated image data. The errors correspond to probability of 68.3 % for the Poisson distribution.

$\cos\theta_{CM}$	-0.4 – 0.1					
Momentum (MeV/c)	300 – 400		400 – 500		500 – 600	
Production Target	H	C	H	C	H	C
Efficiency ε_{scat} (Statistical Error)	.117 (±.036)	.064 (±.023)	.075 (±.013)	.098 (±.021)	.090 (±.032)	.049 (±.013)
N_{scat} (Statistical Error)	0 ($^{+1.15}$)	1 ($^{+2.30}_{-0.83}$)	0 ($^{+1.15}$)	1 ($^{+2.30}_{-0.83}$)	0 ($^{+1.15}$)	1 ($^{+2.30}_{-0.83}$)
$N_{scat}/\varepsilon_{scat}$ (Statistical Error)	0 ($^{+9.8}$)	15.6 ($^{+36.4}_{-14.1}$)	0 ($^{+15.3}$)	10.2 ($^{+23.5}_{-8.7}$)	0 ($^{+12.7}$)	20.5 ($^{+47.5}_{-17.7}$)
Sum of H and C (Statistical Error)	15.6 ($^{+37.7}_{-14.1}$)		10.2 ($^{+28.0}_{-8.7}$)		20.5 ($^{+49.2}_{-17.7}$)	
Sum of All (Statistical Error)	46.3 ($^{+68.0}_{-24.2}$)					

$\cos\theta_{CM}$	0.1 – 0.6					
Momentum (MeV/c)	300 – 400		400 – 500		500 – 600	
Production Target	H	C	H	C	H	C
Efficiency ε_{scat} (Statistical Error)	.164 (±.046)	.137 (±.053)	.156 (±.022)	.101 (±.020)	.189 (±.045)	.066 (±.015)
N_{scat} (Statistical Error)	0 ($^{+1.15}$)	1 ($^{+2.30}_{-0.83}$)	2 ($^{+2.64}_{-1.29}$)	3 ($^{+2.92}_{-1.63}$)	1 ($^{+2.30}_{-0.83}$)	1 ($^{+2.30}_{-0.83}$)
$N_{scat}/\varepsilon_{scat}$ (Statistical Error)	0 ($^{+7.0}$)	7.3 ($^{+17.0}_{-6.6}$)	12.8 ($^{+17.0}_{-8.5}$)	29.7 ($^{+29.5}_{-17.2}$)	5.3 ($^{+12.3}_{-4.6}$)	15.1 ($^{+34.9}_{-12.9}$)
Sum of H and C (Statistical Error)	7.3 ($^{+18.4}_{-6.6}$)		42.5 ($^{+34.0}_{-19.2}$)		20.4 ($^{+37.0}_{-13.7}$)	
Sum of All (Statistical Error)	70.2 ($^{+53.5}_{-24.5}$)					

Table 10: Efficiency corrections for Σ^+ scattering. "H" in production target means H-like Σ^+-production events and "C" means C-like events. N_{scat} denotes the observed number of Σ^+p scatterings. Sums of H-like events and C-like events are shown for each momentum bin and for all the momentum bins.

4.2 Background Subtraction and Cross Section

Σ^+ scattering on the carbon nucleus were background for the Σ^+p scattering. We requested in the analysis that only two branches which corresponded to the Σ^+ track and the recoil proton track were visible at the scattering point. This requirement eliminated background events due to Σ^+–carbon scattering substantially. The number of such background was thus estimated from the cross section for the quasi-free knockout reaction, $^{12}C(p,2p)^{11}B$. The cross section in previous data on the reaction using the incident proton of 644 MeV/c [40] was deduced from the energy distributions calculated from the emitted angles of two protons. It shows that the cross section of the reaction $^{12}C(p,2p)^{11}B$ is 40±20 % of the cross section for proton–proton scattering at the same momentum. These quasi-free events were reduced by the kinematic-fitting process significantly. As the results, the background contamination of Σ^+–carbon scattering in the present data was estimated to be 15±7 %.

4.3 Evaluation of Systematic Errors and the Cross Section

Systematic errors in the derivation of the cross section are caused by uncertainties in the efficiency of the correction for the effective number of Σ^+'s, the efficiency of the correction for the number of Σ^+p scatterings, and the number density of hydrogen nuclei in the SCIFI target, ρ. As described in Section 3.2.5, the momentum resolution of 60 MeV/c or slightly less than 60 MeV/c and the resolution of $\cos\theta_{CM}$ of 0.15 or slightly less than 0.15 were obtained in the present experiment. These values including their systematic uncertainties are smaller than the bin size.

The systematic errors in the efficiencies to calculate the effective number of Σ^+'s and the number of Σ^+p scatterings were partially canceled by dividing the former by the latter in the derivation of the cross section. The event topology of Σ^+p scattering was composed of the topology of Σ^+ scattering including a recoil proton prong and that of Σ^+ decay. Thus, we expected that the systematic errors in the topology of the Σ^+ decay were almost canceled out between the efficiencies for the effective number of Σ^+'s and those for Σ^+p scatterings, although the errors in the scattering topology remained. The actual errors were evaluated with use of the simulation data taking account of the systematic shifts in the flight length estimation for Σ^+ tracks and recoil proton tracks. The shift occurred in the pointing process and caused the largest systematic uncertainty. Since the threshold value of the flight length in the visibility requirement was determined to make such a systematic shift to be less than 1 mm, we artificially added 1 mm or subtracted 1 mm from the observed flight lengths and repeated the same procedure to determine the efficiency. The changes of the efficiencies in this process were regarded as the systematic uncertainty. The systematic errors evaluated in the topology of Σ^+ decay were $\pm$16 %, and those in the topology of Σ^+ scattering and its decay were $\pm$24 %. The error in the cross section, however, was $\pm$14 % because of the cancelation mentioned above. By adding the systematic errors quadratically in the background subtraction, the total systematic error was evaluated to be $\pm$16 %.

In the derivation of the cross section, we considered the target as a block of polystyrene ($(CH)_n$) neglecting PMMA ($C_5H_8O_2$) content in the clad of the scintillating fiber and epoxy content in the glue between SCIFI sheets. The correction corresponds to this effect was in about 1 %.

The differential cross sections for Σ^+p scattering were obtained with use of the numbers of the produced Σ^+'s and the Σ^+p scattering events corrected by the efficiencies after the background subtraction;

$$\frac{d\sigma}{d\Omega} = \begin{cases} 2.2^{+3.2}_{-1.1} \ \text{(mb/sr)} & (-0.4 \le \cos\theta_{CM} < 0.1\ ) \\ 3.3^{+2.5}_{-1.2} \ \text{(mb/sr)} & (\ 0.1 \le \cos\theta_{CM} < 0.6\ ), \end{cases}$$

where the errors are statistical ones. The statistical errors include errors of the real data and ambiguity of the efficiency given by the statistics of the simulated image data. In addition, there are several kinds of systematic errors mentioned above. Overall systematic errors are evaluated to be $\pm$16 % of the obtained cross section. The momentum region of incident Σ^+ is from 300 MeV/c to 600 MeV/c.

5 Discussion

We have identified 11 events of Σ^+p elastic scattering, with which the differential cross section has been obtained. The obtained differential cross sections are shown together with those calculated by the Nijmegen group [41] in Figure 39.

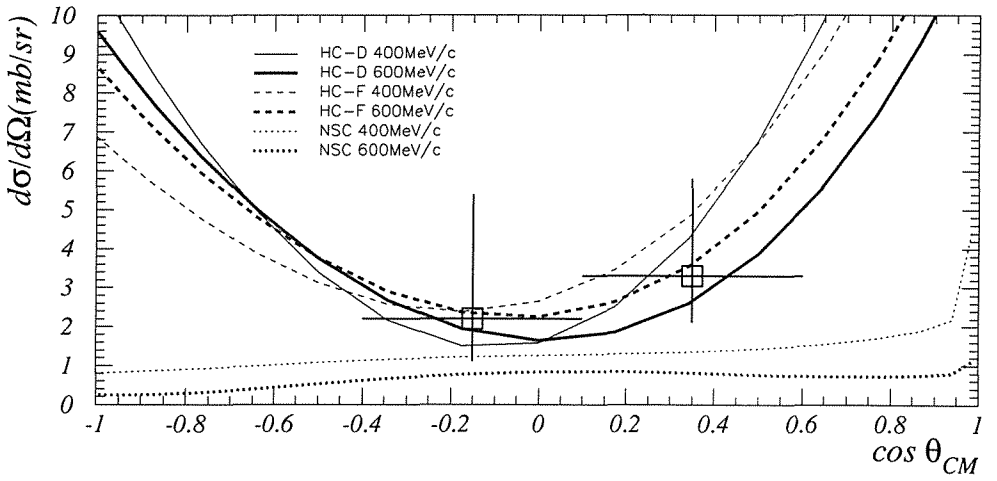

Figure 39: The differential cross section for Σ^+p elastic scattering obtained in this experiment compared with theoretical calculations by the Nijmegen group with the hard-core models D (HC-D), F (HC-F), and the soft-core model (NSC) [41].

The Nijmegen group proposed the models using one-boson-exchange (OBE) picture with a phenomenological core for a short-range repulsive force. They used an infinitely large potential in the short range for the hard-core models, HC-D and HC-F, whereas they used a Gaussian-type potential accounting for the exchange of the Regge trajectories for the soft-core model, NSC.

The differential cross section can be formulated as;

$$\frac{d\sigma}{d\Omega} = A_0 + A_1 \cos\theta_{CM} + A_2 \cos^2\theta_{CM} + \cdots ,$$

where the coefficients A_i are expressed by scattering matrices of partial waves. The calculations of Nijmegen group with the hard-core models have large value of A_2 and show a quadratic behavior which originates in the existence of $^1P_1$ wave. Phase shifts for the $^1P_1$ waves are shown in Table 11. On the other hand, the cross section in the soft-core model is almost isotropic because of smaller contribution of the $^1P_1$ wave. The difference between the total cross sections in the models reflects the difference of the contribution of the $^3S_1$ wave. The $^3S_1$ wave makes a small contribution to the soft-core model, in which the cross section is rather small.

The Kyoto–Niigata group proposed the model, RGM-F, using quark-cluster model

(QCM) based on the resonating group method (RGM) in the short range. Figure 40 shows the differential cross section of our results compared with theoretical calculations by the Kyoto–Niigata group [42]. The $^1P_1$ wave does not make a large contribution to this model. Therefore, the differential cross section does not show a quadratic behavior. The total cross section is larger than those of Nijmegen models because of larger phase shift in the $^3S_1$ wave as shown in Table 11.

model	Nijmegen			Kyoto–Niigata
	HC-D	HC-F	NSC	RGM-F
$^3S_1$ wave (degree)	-17.20	-28.14	-10.46	-36.40
$^1P_1$ wave (degree)	52.25	39.62	4.27	4.87

Table 11: Phase shifts of Σ^+p scattering at 400 MeV/c.

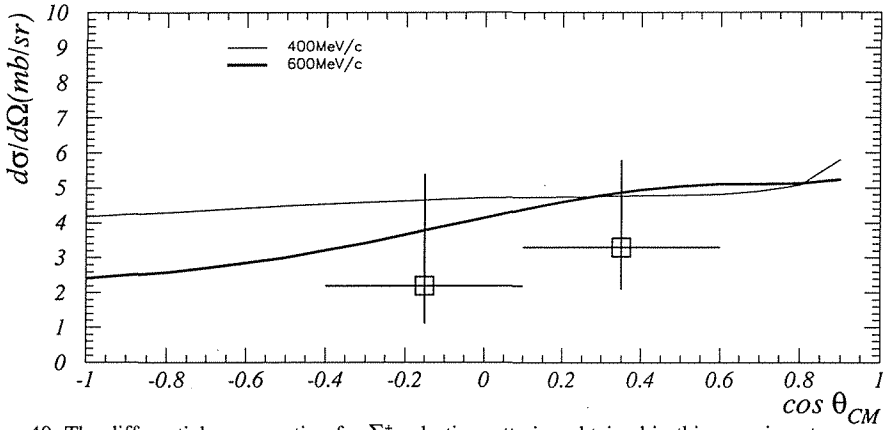

Figure 40: The differential cross section for Σ^+p elastic scattering obtained in this experiment compared with theoretical calculations by the Kyoto–Niigata group with the quark-cluster model (RGM-F) [42].

The present experiment covered the momentum region where the cross section had not been measured before. The obtained cross section is consistent with the prediction of the Nijmegen hard-core models, HC-D and HC-F and the Kyoto–Niigata quark-cluster model within the statistical errors. The present results are less favorite with the predictions of the Nijmegen soft-core model, although the statistics are not sufficient to deny these models.

It should be noted that the present statistics is mainly limited by the number of events taken in the experimental run. It was because this experiment was a pilot experiment performed with new technologies to ensure the possibility of the measurement of hyperon–nucleon scattering cross section, which had never been performed in this energy region due to the experimental difficulties. One of the new techniques which we have applied to this experiment is the detection of the production, scattering and decay of hyperons in the same vertex detector, that is SCIFI detector. In addition, the method of automatic tracking of the image data in the SCIFI detector has been indispensable for the analysis of such large amount of data. In this experiment the Σ^+ production events and Σ^+ decay events are selected by the triggering device of scattered K^+'s in the data acquisition system and the automatic-tracking technique applied to the image data in the SCIFI detector before eye-scanning. About 25 % of the eye-scanned events, that is 6×10^4, contained the produced Σ^+ in the picture. It means that the selections of Σ^+ production and its decay could be performed successfully before eye-scanning. In future, it is not so difficult to

obtain ten times more data on hyperon–nucleon scattering in this energy region using the same techniques as those in this experiment.

The present experiment covers the angular region of $-0.4 \leq \cos\theta_{CM} < 0.6$, whereas it is possible to cover the region of $-0.6 \leq \cos\theta_{CM} < 0.7$ by the present technique with better space resolution if the number of events is sufficient. The coverage of the scattering angle is of vital importance to check the theoretical models, since the angular distribution of hyperon–nucleon scattering is quite sensitive to the contribution of the ${}^1P_1$ partial wave.

Furthermore, the polarization of scattered Σ^+ can also be measured with the present experimental technique, since the decay asymmetry of Σ^+ is observed in the SCIFI detector. The data on the polarization is quite useful for discrimination of various models, because the models mentioned above predict significantly different values for the polarization.

However, for getting better statistics with more experimental data on Σ^+p scattering, we must select the scattering events before eye-scanning by means of further sophisticated automatic-tracking technique.

6 Conclusion

We have measured the differential cross section of Σ^+p elastic scattering in the Σ^+ momentum region of 300 – 600 MeV/c.

The measurement has been performed by the new experimental technique applied to hyperon–nucleon scattering for the first time. The Σ^+'s have been produced in the scintillating-fiber (SCIFI) target in the (π^+,K^+) reaction with the separated π^+ beam of 1.64 GeV/c. Visual images in the SCIFI target have been readout by image-intensifier tubes from two orthogonal directions to provide three-dimensional track information. The readout system of image intensifiers has been triggered by scattered K^+'s which have ensured the hyperon production. The scattering events of Σ^+ in the SCIFI target have been found out by analyzing the visual-image data. For the analysis of the image data, an automatic track recognition program has been developed with which effective background reduction has been achieved. After the reduction of the number of background events by the program, Σ^+p scattering candidates have been selected by eye-scanning. Of those candidates 11 Σ^+p scattering events have been identified.

The results have been compared with theoretical models based on a one-boson-exchange picture by a Nijmegen group and a quark-cluster model by a Kyoto–Niigata group. The obtained cross sections, $2.2^{+3.2}_{-1.1}$(mb/sr) ($-0.4 \leq \cos\theta_{CM} < 0.1$) and $3.3^{+2.5}_{-1.2}$(mb/sr) ($0.1 \leq \cos\theta_{CM} < 0.6$), are consistent with the prediction of the Nijmegen hard-core models and the quark-cluster model, although the statistics have not been so high.

Finally, we would like to stress that the present experiment has established a new method using an automatic-tracking program to measure the cross section for hyperon–nucleon scatterings in the momentum region where other techniques could not be used for the measurement.

Acknowledgements

First of all, I would like to express my sincere thanks to Professor Akira Masaike for his guidance, encouragement and support. I am really grateful to Professor Hideto En'yo for his energetic education and discussion. I am indebted to them also for reading and correcting the manuscript. I wish to thank Professor Kenichi Imai for his advice and suggestions to take over the difficulties.

I sincerely thank all members of E251 collaboration. In particular, I show my appreciation to Dr. Masaharu Ieiri, who was the spokesman of E251, for his management to achieve the experiment and the analysis. I also show my gratitude to S. Mihara and P. Tlustý for their contribution to the operation of chambers and the tracking analysis. I am very grateful to Dr. Y. D. Kim and J.K. Ahn for the studies of basic performance of the SCIFI-target system and the development of the simulation program. I appreciate Dr. Y. Itow, Dr. S. Yamashita and Dr. M. S. Chung for their works for the SCIFI-target and spectrometer system for the previous *H*-dibaryon-search experiment and the present experiment. I am obliged to Professors Y. M. Shin, B. Bassalleck, F. Takeutchi, T. Fukuda and R. Takashima for their expertise, guidances and discussions. I am thankful also to M. Yoshida and Dr. A. Higashi for their collaborations.

I really appreciate supports and helps by members of group for particle and nuclear physics (PN group) in Kyoto University, especially by Dr. N. Saito, H. Funahashi, M. Iinuma and Y. Matsuda to start up the present experiment.

The present experiment and the analysis have been supported by many staff of KEK in accelerator group, beam channel group, online group and computing center. I show my appreciation to Professors T. Sato and Y. Yoshimura for their information about bubble chamber experiment.

The analysis of visual image data obtained from the SCIFI-target system was supported by the idea to recognize tracks with Hough transformation, which was first suggested by Professor A. Ono. I would express special obligation to him.

Theoretical calculations for Σ^+p elastic scattering were provided by courtesy of Professor A. Rijken for the Nijmegen model and Professor Y. Fujiwara for the Kyoto–Niigata model. For the evaluation of Σ^+–carbon scattering, I have obtained many suggestions from Professors A. A. Cowley, T. Noro, H. Sakaguchi and M. Yosoi.

Referrences

[1] M. M. Nagels, Th. A. Rijken, and J. J. de Swart, *Phys. Rev. D* **12**, 744 (1975).
[2] M. M. Nagels, Th. A. Rijken, and J. J. de Swart, *Phys. Rev. D* **17**, 768 (1978).
[3] R. Machleidt, K. Holinde, and Ch. Elster, *Rhys. Rep.* **149**, 1 (1987).
[4] R. Engelmann, H. Filthuth, V. Hepp, and E. Kluge, *Phys. Lett.* 21 587 (1966).
[5] G. Alexander, U. Karchon, A. Shapira, G. Yekutieli, R. Engelmann, H. Filthuth, and W. Lughofer, *Phys. Rev.* **173** 1452 (1968).
[6] B. Sechi-Zorn, B. Kehoe, J. Twitty, and R. A. Burnstein, *Phys. Rev.* **175** 1735 (1968).
[7] G. R. Charlton, J. Badier, E. Barrelet, I. Makarovisch, J. Pernegr, J. R. Hubbard, A. Leveque, C. Louedec, M. Moscoso, and D. Revel, *Phys. Lett.* **32B** 720 (1970).

[8] J. A. Kadyk, G. Alexander, J. H. Chan, P. Gaposchkin, and G. H. Trilling, *Nucl. Phys.* **B27** 13 (1971).
[9] F. Eisele, H. Filthuth, W. Föhlisch, V. Hepp, and G. Zech, *Phys. Lett.* **37B** 204 (1971).
[10] J. M. Hauptman, J. A. Kadyk, and G. H. Trilling, *Nucl. Phys.* **B125** 29 (1977).
[11] M. M. Nagels, Th. A. Rijken, and J. J. de Swart, *Phys. Rev. D* **15**, 2547 (1977).
[12] M. M. Nagels, Th. A. Rijken, and J. J. de Swart, *Phys. Rev. D* **20**, 1633 (1979).
[13] P. M. M. Maessen, Th. A. Rijken, and J. J. de Swart, *Phys. Rev. C* **40**, 2226 (1989).
[14] B. Holzenkamp, K. Holinde, and J. Speth, *Nucl. Phys.* **A500**, 485 (1989).
[15] A. Reuber, K. Holinde, and J. Speth, *Nucl. Phys.* **A570**, 543 (1994).
[16] M. Oka and K. Yazaki, in *Quarks and Nuclei*, edited by W. Weise (World Scientific Publishing, 1984), p. 489.
[17] K. Yazaki, in *Perspectives of Meson Science*, edited by T. Yamazaki, K. Nakai, and K. Nagamine (Elsevier Science Publishers, 1992), p. 795.
[18] M. Oka, K. Ogawa, and S. Takeuchi, in *Properties and Interactions of Hyperons*, Proceedings of the U.S.-Japan Seminar, Maui, Hawaii, 1993, edited by B. F. Gibson, P. D. Barnes, and K. Nakai (World Scientific Publishing, 1994), p. 169.
[19] U. Straub, Z. Y. Zhang, K. Bräuer, A. Faessler, S. B. Khadkikar, and G. Lübeck, *Nucl. Phys.* **A483**, 686 (1988).
[20] U. Straub, Z. Y. Zhang, K. Bräuer, A. Faessler, S. B. Khadkikar, and G. Lübeck, *Nucl. Phys.* **A508**, 385c (1990).
[21] C. Nakamoto, Y. Suzuki, and Y. Fujiwara, *Prog. Theor. Phys.* **94**, 65 (1995).
[22] Y. Fujiwara, C. Nakamoto, and Y. Suzuki, *Prog. Theor. Phys.* **94**, 215 (1995).
[23] Y. Fujiwara, C. Nakamoto, and Y. Suzuki, *Prog. Theor. Phys.* **94**, 353 (1995).
[24] Y. Fujiwara, C. Nakamoto, and Y. Suzuki, *Phys. Rev. Lett.* **76**, 2242 (1996).
[25] C. B. Dover and H. Feshbach, *Ann. Phys. (N.Y.)* **198**, 321 (1990).
[26] C. B. Dover and H. Feshbach, *Ann. Phys. (N.Y.)* **217**, 51 (1992).
[27] A. Ono, private communications.
[28] J. Illingworth and J. Kittler, *Computer Vision, Graphics, and Image Processing* **44**, 87 (1988).
[29] J. K. Ahn *et al.*, *Nucl. Phys.* **A547**, 211c (1992).
[30] J. K. Ahn *et al.*, *Nuovo Cimento* **107A**, 2415 (1994).
[31] J. K. Ahn *et al.*, *Phys. Lett.* B **378**, 53 (1996).
[32] S. Yamashita, *Memoirs of the Faculty of Science, Kyoto University, (Series of Physics, Astrophysics, Geophysics and Chemistry)* **Vol. 39-3**, 349 (1996); Ph.D. thesis, Kyoto University, 1995.
[33] Y. Itow, *Memoirs of the Faculty of Science, Kyoto University, (Series of Physics, Astrophysics, Geophysics and Chemistry)* **Vol. 39-3**, 397 (1996); Ph.D. thesis, Kyoto University, 1995.
[34] A. Yamamoto, H. Ikeda, S. Kurokawa, M. Takasaki, M. Taino, Y. Suzuki, H. Ishii, A. Kusumegi, and H. Hirabayashi, *Nucl. Instr. Meth.* **203**, 35 (1982).
[35] T. K. Ohsuka *et al.*, KEK report 85-10 (1985).
[36] L. Lyons, *Statistics for Nuclear and Particle Physicists* (Cambridge University Press, 1986).
[37] *GEANT – Detector Description and Simulation Tool*, CERN Program Library Long Writeup W5013 (1993).
[38] D. J. Candlin *et al.*, *Nucl. Phys.* **B226**, 1 (1983).
[39] Particle Data Group, *Phys. Rev. D* **50**, 1173 (1994).
[40] A. A. Cowley, J. V. Pilcher, J. J. Lawrie, and D. M. Whittal, *Phys. Rev. C* **40**, 1950 (1989).
[41] Th. A. Rijken, private communications. See also Refs. [11, 12, 13].
[42] Y. Fujiwara and C. Nakamoto, private communications. See also Ref. [22].